Multi-objective optimal design of mechanical metafilters based on principal component analysis

Francesca Fantoni[a,*], Andrea Bacigalupo[b,*], Giorgio Gnecco[c,], Luigi Gambarotta[b,]

[a]DICATAM, University of Brescia, Brescia (Italy)
[b]DICCA, University of Genoa, Genoa (Italy)
[c]AXES, IMT School for Advanced Studies Lucca, Lucca (Italy)

Abstract

In this paper, an advanced computational method is proposed, whose aim is to obtain an approximately optimal design of a particular class of acoustic metamaterials, by combining multi-objective optimization and dimensionality reduction in a novel way. Metamaterials are modeled as beam lattices with internal local resonators coupled with the microstructure through a viscoelastic phase. The dynamics is governed by a set of integro-differential equations, that are transformed into the $\mathcal{Z}$-Laplace space in order to derive an eigenproblem whose solution provides the dispersion relation of the free in-plane propagating Bloch waves. A multi-objective optimization problem is stated, whose aim is to achieve the largest multiplicative trade-off between the bandwidth of the first stop band and the one of the successive pass band in the metamaterial frequency spectrum. Motivated by the multi-dimensionality of the design parameters space, the goal above is achieved by integrating numerical optimization with machine learning. Specifically, the problem is solved by combining a sequential linear programming algorithm with principal component analysis, exploited as a data dimensionality reduction technique. This represents a novel way of applying principal component analysis in connection with multi-objective optimization. Successful performances of the proposed optimization method and its computational savings are demonstrated.

Keywords: Beam lattice metamaterial; Damped wave propagation; Complex-valued frequency spectrum; Gradient-based optimization; Dimensionality reduction.

1. Introduction

Architected materials and metamaterials are composite materials characterized by various smart and unconventional functionalities. They are designed in order to achieve superior effective properties with respect to their ingredient materials. Propelled by both theory and experiments, research efforts conducted in the last decades in the field are huge and focus on different extraordinary aspects such as wave guiding and polarization [1–4], energy transfer, harvesting and sensing [5–12], active and passive control of wave propagation [13–19], extreme lightness and auxeticity [20–25], negative refraction index [26–29], and acoustic filtering [30–35]. Because of the hierarchical nature of such multiphase materials, their microstructural optimization for achieving desired functionalities may involve significant computational resources [36, 37].

---

*Corresponding author
Email addresses: `francesca.fantoni@unibs.it` (Francesca Fantoni), `andrea.bacigalupo@unige.it` (Andrea Bacigalupo)

In this regard, the exceptional advancements in the microengineering and nanotechnologies sectors have caused a fast and revolutionary transformation in the traditional design methodologies for metamaterials and architected materials. Promoted by the onward accelerating growth of accessible computational resources, data-driven approaches have quickly evolved into competitive analyses and design tools as a result of the possibility to interpret and manipulate large datasets using artificial intelligence techniques. Nowadays these tools represent a useful support or even a valid alternative to conventional model-driven methodologies [38–43]. Machine learning algorithms have revealed highly beneficial in resolving challenging mathematical and computational problems afflicted by high dimensions, strong nonlinearities, and the existence of multiple solutions, and constraints [44]. Among them, Principal Component Analysis (PCA) is a well-known data dimensionality reduction technique [45, 46]. Loosely speaking, it works by projecting a dataset onto a subspace having a reduced dimension, which is generated by a subset of so-called principal directions. Among all subspaces having a certain reduced dimension, the one generated by the principal directions identified by PCA minimizes the mean squared error of approximation of its training dataset. Although there exist several classical applications of PCA to materials science [47], it was recently shown by the authors [48] that PCA can also be successfully exploited in connection with constrained multi-objective optimization problems, since instead of exploiting the true gradient of the constrained objective function, an approximation of that gradient can be used, this last obtained from the application of PCA to the properly sampled field of gradient directions. According to the authors' experience, this is a non-standard, almost unexplored, but potentially quite interesting way of using PCA in connection with multi-objective optimization (the case of single-objective optimization was briefly considered by the authors in a recent conference work [49]). It is worth mentioning that a related application of PCA to image gradient orientations is also reported in the literature on image processing [50].

Departing from this stimulating framework, this paper focuses on a particular class of metamaterials, identified as mechanical, or acoustic metamaterials with the goal of optimizing specific spectral properties. Acoustic metamaterials, whose mechanical model departs from a beam lattice description, are characterized by a periodic topology and a microstructure enriched by massive oscillators acting as tunable local resonators. Their tunability and the consequent frequency-dispersive behavior of various properties (such as mass density [51], bulk modulus [52] or both [53]) results in a dynamic interaction with the microstructure, causing the opening of band gaps in the relative frequency spectrum [19, 54]. The bandwidth of these band gaps is nearly directly proportional to the oscillator mass and the central frequency almost approximates the oscillator natural one [55–60]. Local resonance, therefore, can be wisely exploited in order to attain different desirable effects fascinating from both the fundamental and practical points of view such as filtering, transmission amplification, image lensing, modal localization, wave trapping, and edging [61–64]. In this regard, this paper is devoted to attaining the largest multiplicative trade-off between the first band gap and the pass band of optical branches of acoustic metamaterials, whose local resonators are coupled to the periodic non-dissipative microstructure through a viscoelastic phase [65]. Resulting linear integro-differential equations of motion are described in Section 2. In the same Section, thanks to the periodicity of the medium at hand, wave propagation of in-plane Bloch waves is investigated according to the Floquet-Bloch theory, after the transformation of the governing equations in the $\mathcal{Z}$-Laplace space. The dispersion relation is obtained by solving a non-polynomial eigenproblem, properly de-rationalized, and determining complex frequencies in terms of real wavevectors (temporal damping). The achievement of the optimal filtering performance is mathematically formalized in Section 3, where the solution of a
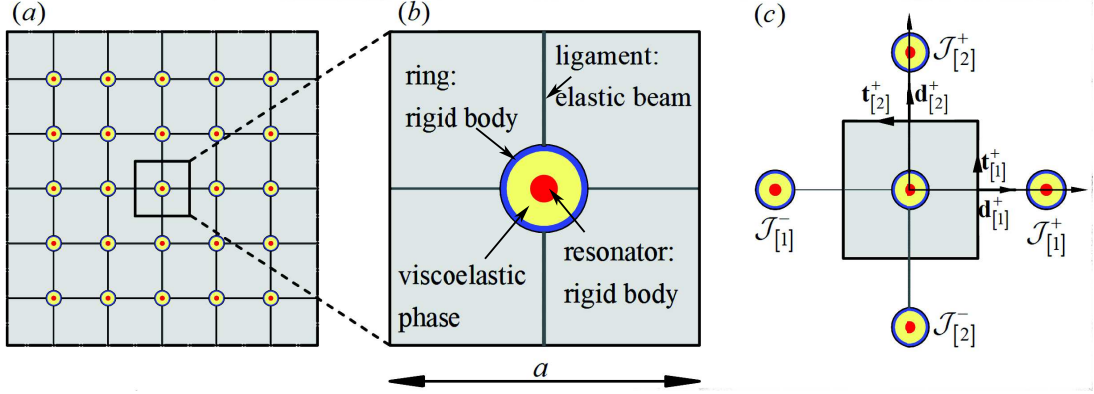
Figure 1: Mechanical model for the beam lattice metamaterial: (a) quadrilateral cellular topology, (b) periodic cell of size a, (c) coordination lines.

unilaterally-constrained maximization problem is sought for. Real-valued microstructural parameters are selected as optimization variables and a subset of constraints is taken into account in the corresponding penalized objective function by means of a suitable penalty term. Numerical optimization is performed through a gradient-based optimization algorithm, where PCA is exploited in order to accurately approximate the penalized objective function gradient directions. The computational efficiency of the adopted machine learning-based algorithm is demonstrated and discussed in Section 4, where successful performances of the optimization method in the design of mechanical metafilters are shown. Final remarks are reported in Section 5.

2. Mechanical model of a viscoelastic beam lattice metamaterial

Mechanical metamaterials with viscoelastic resonators are characterized by a periodic microstructure based on spatial repetition of a certain cellular topology along $n/2$ lattice coordination lines, with n an even integer number representing the lattice coordination number. If the periodic cell, whose characteristic size is denoted as a, is centrosymmetric and quadrilateral, its coordination number is $n = 4$ (see figure 1). Each cell is characterized by a stiff ring having a mean radius equal to R, mass M_1, and rotational inertia J_1. With reference to the configuration node located at its centroid, the ring is modeled as a rigid body whose in-plane motion is described by displacement vector $\mathbf{u}$ and rotation ϕ. n identical light and flexible massless ligaments having length $L = a - 2R$ and width w connect each massive ring to the adjacent ones.

They are modeled as linear unshearable beams having Young modulus E and their joints with the stiff rings are assumed as perfectly rigid. Local resonance is obtained by enhancing each stiff ring with a co-centered heavy stiff disk having radius r, mass M_2, and rotational inertia J_2. The local resonator is embedded in a soft annular matrix exhibiting a viscoelastic material behavior and characterized by the time-dependent relaxation function $k_d(t)$ for the relative ring-resonator displacement and $k_a(t)$ for the relative ring-resonator rotation. Each massive resonator is modeled as a rigid body whose in-plane motion is described by displacement vector $\mathbf{v}$ and rotation θ, again with reference to the configuration node located at the disk centroid, that results to be geometrically coincident with the heavy ring one (two-node lattice point). Finally, the mechanical model of the periodic cell is assumed to have a unitary depth d along the out-of-plane direction. In-plane external nodal force vector $\mathbf{f}$ and moment g represent the dynamic

3

excitations acting on the ring, while the local resonator is considered as unloaded. If ω_r and L_r denote, respectively, a known reference frequency and a known reference length, according to [65], the following dimensionless variables can be conveniently defined

$$\tilde{t} = \omega_r t, \qquad \tilde{\tau} = \omega_r \tau, \qquad \tilde{\mathbf{u}} = \frac{\mathbf{u}}{L_r}, \qquad \tilde{\mathbf{v}} = \frac{\mathbf{v}}{L_r}, \qquad \tilde{\mathbf{f}} = \frac{\mathbf{f}}{\omega_r^2 M_1 L_r}, \qquad \tilde{g} = \frac{g}{\omega_r^2 M_1 L_r^2}, \qquad (1)$$

together with the following suitable number of dimensionless mechanical parameters

$$\varrho^2 = \frac{M_2}{M_1}, \qquad \chi_1^2 = \frac{J_1}{M_1 L_r^2} = \frac{R^2}{L_r^2}, \qquad \chi_2^2 = \frac{J_2}{M_2 L_r^2} = \frac{r^2}{2L_r^2}, \qquad \eta^2 = \frac{Ea}{\omega_r^2 M_1},$$

$$\kappa_d = \frac{k_d}{Ea}, \qquad \kappa_a = \frac{k_a}{EaL_r^2}, \qquad \alpha = \frac{a}{L_r}, \qquad \delta = \frac{d}{a}, \qquad \mu = \frac{w}{L}. \qquad (2)$$

The forced dynamics of the beam lattice metamaterial is described by a set of integro-differential equations of motion, whose dimensionless form reads

$$\ddot{\tilde{\mathbf{u}}}_{\mathcal{J}} + \int_{-\infty}^{\tilde{t}} \eta^2 \kappa_d(\tilde{t} - \tilde{\tau}) \tfrac{d}{d\tilde{\tau}} (\tilde{\mathbf{u}}_{\mathcal{J}} - \tilde{\mathbf{v}}_{\mathcal{J}}) \, d\tilde{\tau} + \sum_{\mathcal{P}_{[j]}} \left(\tilde{\mathbf{r}}^+_{\mathcal{J}_{[j]}} + \tilde{\mathbf{r}}^-_{\mathcal{J}_{[j]}} \right) = \tilde{\mathbf{f}}_{\mathcal{J}},$$

$$\chi_1^2 \ddot{\phi}_{\mathcal{J}} + \int_{-\infty}^{\tilde{t}} \eta^2 \kappa_a(\tilde{t} - \tilde{\tau}) \tfrac{d}{d\tilde{\tau}} (\phi_{\mathcal{J}} - \theta_{\mathcal{J}}) \, d\tilde{\tau} + \sum_{\mathcal{P}_{[j]}} \left(\tilde{c}^+_{\mathcal{J}_{[j]}} + \tilde{c}^-_{\mathcal{J}_{[j]}} \right) = \tilde{g}_{\mathcal{J}},$$

$$\varrho^2 \ddot{\tilde{\mathbf{v}}}_{\mathcal{J}} + \int_{-\infty}^{\tilde{t}} \eta^2 \kappa_d(\tilde{t} - \tilde{\tau}) \tfrac{d}{d\tilde{\tau}} (\tilde{\mathbf{v}}_{\mathcal{J}} - \tilde{\mathbf{u}}_{\mathcal{J}}) \, d\tilde{\tau} = \mathbf{0},$$

$$\varrho^2 \chi_2^2 \ddot{\theta}_{\mathcal{J}} + \int_{-\infty}^{\tilde{t}} \eta^2 \kappa_a(\tilde{t} - \tilde{\tau}) \tfrac{d}{d\tilde{\tau}} (\theta_{\mathcal{J}} - \phi_{\mathcal{J}}) \, d\tilde{\tau} = 0. \qquad (3)$$

In equation (3), dots denote derivatives with respect to dimensionless time $\tilde{t}$, $\mathcal{J} = (i_1, ..., i_{n/2})$ represents the set of lattice coordination lines and it is used to select a specific node of the lattice, while $\mathcal{J}_{[j]} = (i_1, ..., i_j, ..., i_{n/2})$ identifies the i-th node along coordination line j. $\mathcal{P}_{[j]}$ allows identifying the j−th coordination line since it collects the integer j-values belonging to the range $[1, n/2]$. Dimensionless internal forces acting on lattice node $\mathcal{J}_{[j]}$ are expressed as

$$\tilde{\mathbf{r}}^+_{\mathcal{J}_{[j]}} = \tilde{\mathbf{K}}^+_{[j]} (\tilde{\mathbf{u}}_{\mathcal{J}_{[j]}} - \tilde{\mathbf{u}}_{\mathcal{J}^+_{[j]}}) + \tilde{\mathbf{k}}^+_{[j]} (\phi_{\mathcal{J}_{[j]}} + \phi_{\mathcal{J}^+_{[j]}}),$$

$$\tilde{\mathbf{r}}^-_{\mathcal{J}_{[j]}} = \tilde{\mathbf{K}}^-_{[j]} (\tilde{\mathbf{u}}_{\mathcal{J}_{[j]}} - \tilde{\mathbf{u}}_{\mathcal{J}^-_{[j]}}) + \tilde{\mathbf{k}}^-_{[j]} (\phi_{\mathcal{J}_{[j]}} + \phi_{\mathcal{J}^-_{[j]}}),$$

$$\tilde{c}^+_{\mathcal{J}_{[j]}} = \tilde{\mathbf{k}}^+_{[j]} \cdot (\tilde{\mathbf{u}}_{\mathcal{J}_{[j]}} - \tilde{\mathbf{u}}_{\mathcal{J}^+_{[j]}}) + \tilde{K}_a (\phi_{\mathcal{J}_{[j]}} + \phi_{\mathcal{J}^+_{[j]}}) + \tilde{K}_\ell (\phi_{\mathcal{J}_{[j]}} - \phi_{\mathcal{J}^+_{[j]}}),$$

$$\tilde{c}^-_{\mathcal{J}_{[j]}} = \tilde{\mathbf{k}}^-_{[j]} \cdot (\tilde{\mathbf{u}}_{\mathcal{J}_{[j]}} - \tilde{\mathbf{u}}_{\mathcal{J}^-_{[j]}}) + \tilde{K}_a (\phi_{\mathcal{J}_{[j]}} + \phi_{\mathcal{J}^-_{[j]}}) + \tilde{K}_\ell (\phi_{\mathcal{J}_{[j]}} - \phi_{\mathcal{J}^-_{[j]}}), \qquad (4)$$

where stiffness coefficients have the following dimensionless form

$$\tilde{\mathbf{K}}^\pm_{[j]} = \eta^2 \delta\mu \left[\left(\mathbf{d}^\pm_{[j]} \otimes \mathbf{d}^\pm_{[j]} \right) + \mu^2 \left(\mathbf{t}^\pm_{[j]} \otimes \mathbf{t}^\pm_{[j]} \right) \right], \quad \tilde{\mathbf{k}}^\pm_{[j]} = \tfrac{1}{2}\alpha\eta^2\delta\mu^3 \mathbf{t}^\pm_{[j]}, \quad \tilde{K}_a = \frac{1}{4}\alpha^2\eta^2\delta\mu^3, \quad \tilde{K}_\ell = \frac{1}{12}(\alpha - 2\chi_1)^2\eta^2\delta\mu^3.$$

$$(5)$$

According to the adopted notation, in equation (4), $\mathcal{J}^\pm_{[j]} = (i_1, ..., i_j \pm 1, ..., i_{n/2})$ is the set of coordination lines that allows to identify the $i \pm 1$ node of the lattice along coordination line j. Dimensionless time-dependent relaxation functions can be expressed in terms of the Prony series as [66]

$$\kappa_d(\tilde{t}) = \kappa_{de} \left[1 + \sum_{n=1}^{N_p} \beta_d^n \exp\left(-\frac{\eta\tilde{t}}{\tilde{t}_r^n} \right) \right], \qquad \kappa_a(\tilde{t}) = \kappa_{ae} \left[1 + \sum_{n=1}^{N_p} \beta_a^n \exp\left(-\frac{\eta\tilde{t}}{\tilde{t}_r^n} \right) \right], \qquad (6)$$

where κ_{de} and κ_{ae} refer to nondimensional long term response of the material for the relative displacement and relative rotation, respectively, while β_d^n and β_a^n represent the corresponding n-th viscosity ratios. The n-th dimensionless relaxation time that governs the exponential decay rate of the relative relaxation function is denoted in equation (6) as $\tilde{t}_r^n$.

2.1. Free propagation of in-plane Bloch waves

In order to investigate the propagation of elastic Bloch waves inside the metamaterial, a bilateral Laplace transform in time and a bilateral $\mathcal{Z}$-transform in space are applied to the dimensionless equations of motion (3). If $\tilde{q}(\tilde{t})$ is a real-valued, non dimensional, time-dependent function, denoting with $\tilde{s} = s/\omega_r$ the dimensionless complex Laplace argument, bilateral Laplace transform of $\tilde{q}(\tilde{t})$ is defined as

$$\mathcal{L}[\tilde{q}(\tilde{t})] = \hat{q}(\tilde{s}) = \int_{\mathbb{R}} \tilde{q}(\tilde{t}) \exp(-\tilde{s}\tilde{t}) \, d\tilde{t}, \tag{7}$$

with $\hat{q}(\tilde{s}) : \mathbb{C} \to \mathbb{C}$. Accounting for the spatial periodicity of the lattice, bilateral $\mathcal{Z}$-transform [67, 68] of function $q_{\mathcal{J}} : \mathbb{Z}^{n/2} \to \mathbb{C}$ is defined as

$$\mathcal{Z}[q_{\mathcal{J}}] = \mathcal{Z}[q_{(i_1,\dots,i_{n/2})}] = \sum_{\mathcal{J} \in \mathbb{Z}^{n/2}} q_{(i_1,\dots,i_{n/2})} z_1^{-i_1} \dots z_{n/2}^{-i_{n/2}} = \check{q}(z_1 \dots z_{n/2}) = \check{q}(\mathbf{z}), \tag{8}$$

with $\mathbf{z} = (z_1 \dots z_{n/2})^T \in \mathbb{C}^{n/2}$ and $\check{q}(\mathbf{z})$ a complex-valued function. Making use of the Laplace transform properties $\mathcal{L}[\frac{\partial^n \tilde{q}(\tilde{t})}{\partial \tilde{t}^n}] = \tilde{s}^n \mathcal{L}[\tilde{q}(\tilde{t})]$ and $\mathcal{L}[\tilde{q}_1(\tilde{t}) * \tilde{q}_2(\tilde{t})] = \mathcal{L}[\tilde{q}_1(\tilde{t})]\mathcal{L}[\tilde{q}_2(\tilde{t})]$, and of the $\mathcal{Z}$-transform property $\mathcal{Z}[q_{(i_1 \pm m_1,\dots,i_{n/2} \pm m_{n/2})}] = z_1^{\pm m_1} \dots z_{n/2}^{\pm m_{n/2}} \mathcal{Z}[q_{(i_1,\dots i_{n/2})}]$, equations (3) are transformed into

$$\tilde{s}^2 \mathring{\mathbf{u}}(\mathbf{z}, \tilde{s}) + \tilde{s}\eta^2 \hat{\kappa}_d(\tilde{s})(\mathring{\mathbf{u}}(\mathbf{z}, \tilde{s}) - \mathring{\mathbf{v}}(\mathbf{z}, \tilde{s})) + \sum_{\mathcal{P}_{[j]}} \left(\mathring{\mathbf{r}}^+_{\mathcal{J}_{[j]}} + \mathring{\mathbf{r}}^-_{\mathcal{J}_{[j]}} \right) = \mathring{\mathbf{f}}(\mathbf{z}, \tilde{s}),$$

$$\chi_1^2 \tilde{s}^2 \mathring{\phi}(\mathbf{z}, \tilde{s}) + \tilde{s}\eta^2 \hat{\kappa}_a(\tilde{s})(\mathring{\phi}(\mathbf{z}, \tilde{s}) - \mathring{\theta}(\mathbf{z}, \tilde{s})) + \sum_{\mathcal{P}_{[j]}} \left(\mathring{c}^+_{\mathcal{J}_{[j]}} + \mathring{c}^-_{\mathcal{J}_{[j]}} \right) = \mathring{g}(\mathbf{z}, \tilde{s}),$$

$$\varrho^2 \tilde{s}^2 \mathring{\mathbf{v}}(\mathbf{z}, \tilde{s}) + \tilde{s}\eta^2 \hat{\kappa}_d(\tilde{s}) (\mathring{\mathbf{v}}(\mathbf{z}, \tilde{s}) - \mathring{\mathbf{u}}(\mathbf{z}, \tilde{s})) = \mathbf{0},$$

$$\varrho^2 \tilde{s}^2 \chi_2^2 \mathring{\theta}(\mathbf{z}, \tilde{s}) + \tilde{s}\eta^2 \hat{\kappa}_a(\tilde{s})(\mathring{\theta}(\mathbf{z}, \tilde{s}) - \mathring{\phi}(\mathbf{z}, \tilde{s})) = 0, \tag{9}$$

where $\mathring{q}(\mathbf{z}, \tilde{s}) = \mathcal{Z}[\hat{q}_{\mathcal{J}}(\tilde{s})] = \mathcal{Z}[\mathcal{L}[\tilde{q}_{\mathcal{J}}(\tilde{t})]]$ stands for the $\mathcal{Z}$-transform of the Laplace transform of function $\tilde{q}_{\mathcal{J}}(\tilde{t})$. Doubly-transformed inter-cellular internal forces in equation (9) acting on the $\mathcal{J}$-th node have the following expressions

$$\mathring{\mathbf{r}}^+_{\mathcal{J}_{[j]}} = (1 - z_j) \tilde{\mathbf{K}}^+_{[j]} \mathring{\mathbf{u}}(\mathbf{z}, \tilde{s}) + (1 + z_j) \tilde{\mathbf{k}}^+_{[j]} \mathring{\phi}(\mathbf{z}, \tilde{s}),$$

$$\mathring{\mathbf{r}}^-_{\mathcal{J}_{[j]}} = (1 - z_j^{-1}) \tilde{\mathbf{K}}^-_{[j]} \mathring{\mathbf{u}}(\mathbf{z}, \tilde{s}) + (1 + z_j^{-1}) \tilde{\mathbf{k}}^-_{[j]} \mathring{\phi}(\mathbf{z}, \tilde{s}),$$

$$\mathring{c}^+_{\mathcal{J}_{[j]}} = (1 - z_j) \tilde{\mathbf{k}}^+_{[j]} \cdot \mathring{\mathbf{u}}(\mathbf{z}, \tilde{s}) + (1 - z_j) \tilde{K}_a \mathring{\phi}(\mathbf{z}, \tilde{s}) + (1 - z_j) \tilde{K}_\ell \mathring{\phi}(\mathbf{z}, \tilde{s}),$$

$$\mathring{c}^-_{\mathcal{J}_{[j]}} = (1 - z_j^{-1}) \tilde{\mathbf{k}}^-_{[j]} \cdot \mathring{\mathbf{u}}(\mathbf{z}, \tilde{s}) + (1 - z_j^{-1}) \tilde{K}_a \mathring{\phi}(\mathbf{z}, \tilde{s}) + (1 - z_j^{-1}) \tilde{K}_\ell \mathring{\phi}(\mathbf{z}, \tilde{s}). \tag{10}$$

In equation (9), $\hat{\kappa}_d(\tilde{s})$ and $\hat{\kappa}_a(\tilde{s})$ refer to the dimensionless transformed relaxation functions for the relative displacement and relative rotation, respectively. The linear system of algebraic equations (9) can be concisely expressed in matrix form as

$$\mathbf{C}(\mathbf{z}, \tilde{s}) \mathring{\mathbf{U}}(\mathbf{z}, \tilde{s}) = \mathring{\mathbf{F}}(\mathbf{z}, \tilde{s}), \tag{11}$$

where vectors $\mathring{\mathbf{U}}(\mathbf{z}, \tilde{s}) = \left(\mathring{\mathbf{u}}(\mathbf{z}, \tilde{s}) \, \mathring{\phi}(\mathbf{z}, \tilde{s}) \, \mathring{\mathbf{v}}(\mathbf{z}, \tilde{s}) \, \mathring{\theta}(\mathbf{z}, \tilde{s})\right)^T$ and $\mathring{\mathbf{F}}(\mathbf{z}, \tilde{s}) = \left(\mathring{\mathbf{f}}(\mathbf{z}, \tilde{s}) \, \mathring{g}(\mathbf{z}, \tilde{s}) \, \mathbf{0} \, 0\right)^T$ collect the transformed six components of displacement and rotation and external forces and moments, respectively. Dynamic stiffness matrix $\mathbf{C}(\mathbf{z}, \tilde{s})$, therefore, is expressed as

$$\mathbf{C}(\mathbf{z}, \tilde{s}) = \begin{bmatrix} \mathbf{A}(\mathbf{z}, \tilde{s}) + \tilde{s}^2\mathbf{I} & \mathbf{a}^-(\mathbf{z}) & -\tilde{s}\eta^2\hat{\kappa}_d(\tilde{s})\mathbf{I} & \mathbf{0} \\ \mathbf{a}^+(\mathbf{z}) & B(\mathbf{z}, \tilde{s}) + \tilde{s}^2\chi_1^2 & \mathbf{0} & -\tilde{s}\eta^2\hat{\kappa}_a(\tilde{s}) \\ -\tilde{s}\eta^2\hat{\kappa}_d(\tilde{s})\mathbf{I} & \mathbf{0} & \tilde{s}\eta^2\hat{\kappa}_d(\tilde{s})\mathbf{I} + \tilde{s}^2\varrho^2\mathbf{I} & \mathbf{0} \\ \mathbf{0} & -\tilde{s}\eta^2\hat{\kappa}_a(\tilde{s}) & \mathbf{0} & \tilde{s}\eta^2\hat{\kappa}_a(\tilde{s}) + \tilde{s}^2\varrho^2\chi_2^2 \end{bmatrix}, \tag{12}$$

where, denoting with $\mathbf{I}$ the identity matrix, one has

$$\mathbf{A}(\mathbf{z}, \tilde{s}) = \tilde{s}\eta^2\hat{\kappa}_d(\tilde{s})\mathbf{I} + \sum_{\mathcal{P}_{[j]}}\left[(1 - z_j)\tilde{\mathbf{K}}_{[j]}^+ + (1 - z_j^{-1})\tilde{\mathbf{K}}_{[j]}^-\right],$$

$$\mathbf{a}^-(\mathbf{z}) = \sum_{\mathcal{P}_{[j]}}\left[(1 + z_j)\tilde{\mathbf{k}}_{[j]}^+ + (1 + z_j^{-1})\tilde{\mathbf{k}}_{[j]}^-\right],$$

$$\mathbf{a}^+(\mathbf{z}) = \sum_{\mathcal{P}_{[j]}}\left[(1 - z_j)\tilde{\mathbf{k}}_{[j]}^+ + (1 - z_j^{-1})\tilde{\mathbf{k}}_{[j]}^-\right],$$

$$B(\mathbf{z}, \tilde{s}) = \tilde{s}\eta^2\hat{\kappa}_a(\tilde{s}) + \sum_{\mathcal{P}_{[j]}}\left[(1 + z_j)\tilde{K}_a + (1 - z_j)\tilde{K}_\ell + (1 + z_j^{-1})\tilde{K}_a + (1 - z_j^{-1})\tilde{K}_\ell\right]. \tag{13}$$

Denoting with $\mathbf{n}_{[j]}$ the unit vector along the j-th coordination line, which, because of cellular topology at hand, coincides with unit vector $\mathbf{d}_{[j]}$, complex variables z_j, with $j = 1, ..., n/2$ can be mapped on the unit circle as $z_j = \exp\left(i\left(\mathbf{n}_{[j]} \cdot \mathbf{b}\right)\right)$, where $\mathbf{b} = (\beta_1 \, \beta_2)^T$ represents the dimensionless wavevector. System (11), therefore, can be written making explicit its $\mathbf{b}$-dependence as

$$\mathbf{C}(\mathbf{b}, \tilde{s}) \, \mathring{\mathbf{U}}(\mathbf{b}, \tilde{s}) = \mathring{\mathbf{F}}(\mathbf{b}, \tilde{s}). \tag{14}$$

With the aim of investigating temporal damping for the metamaterial at hand, dispersion relation $\tilde{s}(\mathbf{b})$ is sought for, describing the behavior of the complex dimensionless frequency in terms of the real-valued dimensionless wavevector, this last belonging to the dimensionless first Brillouin zone. From equation (14), the dispersion relation is obtained from the solution of the rational eigenvalue problem

$$\mathbf{C}(\mathbf{b}, \tilde{s}) \, \mathring{\mathbf{U}}(\mathbf{b}, \tilde{s}) = \mathbf{0}, \tag{15}$$

where vector $\mathring{\mathbf{F}}(\mathbf{b}, \tilde{s}) = \mathbf{0}$ because of the imposed free wave propagation condition. As usual, non-trivial solutions $\mathring{\mathbf{U}}(\mathbf{b}, \tilde{s})$ of the homogeneous equation of motion (15) are determined by imposing the singularity of system matrix $\mathbf{C}(\mathbf{b}, \tilde{s})$ and complex eigenvalues $\tilde{s}$ are the roots of characteristic equation $\det(\mathbf{C}(\mathbf{b}, \tilde{s})) = 0$. Their real and imaginary components are associated to damping and propagation modes, respectively, of damped waves propagating inside the medium.

2.2. De-rationalization of the rational eigenvalue problem

In order to find the exact solution $\tilde{s}(\mathbf{b})$ of the rational eigenvalue problem (15), a de-rationalization procedure is adopted [69]. To this aim, equation (15) is conveniently rewritten detailing the dependence of terms on dimensionless complex frequency $\tilde{s}$ as

$$\left(\tilde{s}^2 \mathbf{M} + \frac{\eta^2}{\prod_{i=1}^{N_p}\left(\frac{\eta}{\tilde{t}_r}+\tilde{s}\right)}\left(\tilde{s}^{N_p}\,\mathbf{G}_{N_p}+...+\mathbf{G}_0\right)+\mathbf{H}(\mathbf{b})\right)\mathring{\mathbf{U}}(\mathbf{b},\tilde{s})=\mathbf{0},\tag{16}$$

where it is worth recalling that N_p represents the number of terms considered in the Prony series (6). Denoting with $\mathbf{S}(\tilde{s}) = \frac{\eta^2}{\prod_{i=1}^{N_p}(\eta/\tilde{t}_r+\tilde{s})}\mathbf{I}$, its inverse can be wisely written as

$$\mathbf{S}^{-1}(\tilde{s}) = \frac{1}{\eta^2}\prod_{i=1}^{N_p}\left(\tilde{s}+\frac{\eta}{\tilde{t}_r}\right)\mathbf{I} = \frac{1}{\eta^2}\sum_{i=0}^{N_p}\left(\alpha_i\tilde{s}^i\right)\mathbf{I}.\tag{17}$$

Coefficients α_i of equation (17) are such that $\alpha_{N_p} = 1$ and

$$\alpha_{N_p-k} = (-1)^k \sum_{\mathcal{P}_k^{[1,N_p]}(j_1,...,j_k)}\left(\prod_{i=1}^{k}\left(-\frac{\eta}{\tilde{t}_r^{j_i}}\right)\right),\tag{18}$$

being $\mathcal{P}_k^{[1,N_p]}(j_1,...,j_k)$ the set of all combinations of order k of indexes $j_1,...,j_k$ in the range $[1,N_p]$, with integer $k \in [1,N_p]$ (see [70] for details). Examples of application of equation (18) can be found in Section A.2 of the supplementary material. In this way, equation (16) takes the form of a polynomial eigenvalue problem expressed as

$$\left(\sum_{i=0}^{N_p}\tilde{s}^i\begin{bmatrix}\mathbf{0} & \mathbf{0} \\ \mathbf{G}_i & -\frac{\alpha_i}{\eta^2}\mathbf{I}\end{bmatrix}+\tilde{s}^2\begin{bmatrix}\mathbf{M} & \mathbf{0} \\ \mathbf{0} & \mathbf{0}\end{bmatrix}+\begin{bmatrix}\mathbf{H}(\mathbf{b}) & \mathbf{I} \\ \mathbf{0} & \mathbf{0}\end{bmatrix}\right)\begin{bmatrix}\mathring{\mathbf{U}}(\mathbf{b},\tilde{s}) \\ \mathring{\mathbf{Q}}(\mathbf{b},\tilde{s})\end{bmatrix}=\begin{bmatrix}\mathbf{0} \\ \mathbf{0}\end{bmatrix},\tag{19}$$

being $\mathring{\mathbf{Q}}(\mathbf{b},\tilde{s}) = \left(\mathbf{S}(\tilde{s})\sum_{i=0}^{N_p}\tilde{s}^i\mathbf{G}_i\right)\mathring{\mathbf{U}}(\mathbf{b},\tilde{s}) = \eta^2\left(\sum_{i=0}^{N_p}\tilde{s}^i\alpha_i\right)^{-1}\mathbf{I}\left(\sum_{i=0}^{N_p}\tilde{s}^i\mathbf{G}_i\right)\mathring{\mathbf{U}}(\mathbf{b},\tilde{s})$ an auxiliary vectorial variable. Characteristic equation associated to polynomial eigenvalue problem (19), which could also be linearized following, for example, a procedure analogous to that exploited in [71, 72] for the linearization of higher-order ordinary differential equations, allows determining the complex frequency spectrum of the periodic metamaterial. Considering from now on Prony series (6) truncated at $N_p = 1$, matrices involved in system (19) read

$$\mathbf{M}=\begin{bmatrix}\mathbf{I} & \mathbf{0} & \mathbf{0} & \mathbf{0} \\ \mathbf{0} & \chi_1^2 & \mathbf{0} & \mathbf{0} \\ \mathbf{0} & \mathbf{0} & \varrho^2\mathbf{I} & \mathbf{0} \\ \mathbf{0} & \mathbf{0} & \mathbf{0} & \varrho^2\chi_2^2\end{bmatrix},\quad \mathbf{G}_1=\begin{bmatrix}\kappa_{de}(1+\beta_d)\mathbf{I} & \mathbf{0} & -\kappa_{de}(1+\beta_d)\mathbf{I} & \mathbf{0} \\ \mathbf{0} & \kappa_{ae}(1+\beta_a) & \mathbf{0} & -\kappa_{ae}(1+\beta_a) \\ -\kappa_{de}(1+\beta_d)\mathbf{I} & \mathbf{0} & \kappa_{de}(1+\beta_d)\mathbf{I} & \mathbf{0} \\ \mathbf{0} & -\kappa_{ae}(1+\beta_a) & \mathbf{0} & \kappa_{ae}(1+\beta_a)\end{bmatrix},$$

$$\mathbf{G}_0=\frac{\eta}{\tilde{t}_r}\begin{bmatrix}\kappa_{de}\mathbf{I} & \mathbf{0} & -\kappa_{de}\mathbf{I} & \mathbf{0} \\ \mathbf{0} & \kappa_{ae} & \mathbf{0} & -\kappa_{ae} \\ -\kappa_{de}\mathbf{I} & \mathbf{0} & \kappa_{de}\mathbf{I} & \mathbf{0} \\ \mathbf{0} & -\kappa_{ae} & \mathbf{0} & \kappa_{ae}\end{bmatrix},\quad \mathbf{H}(\mathbf{b})=\begin{bmatrix}\mathbf{A}_0(\mathbf{b}) & \mathbf{a}^-(\mathbf{b}) & -\eta^2\kappa_{de}\mathbf{I} & \mathbf{0} \\ \mathbf{a}^+(\mathbf{b}) & B_0(\mathbf{b}) & \mathbf{0} & -\eta^2\kappa_{ae} \\ -\eta^2\kappa_{de}\mathbf{I} & \mathbf{0} & \eta^2\kappa_{de}\mathbf{I} & \mathbf{0} \\ \mathbf{0} & -\eta^2\kappa_{ae} & \mathbf{0} & \eta^2\kappa_{ae}\end{bmatrix},\tag{20}$$

with

$$\mathbf{A}_0(\mathbf{b}) = \eta^2 \kappa_{de} \mathbf{I} + \sum_{\mathcal{P}_{[j]}} \Big[(1 - \exp[\imath(\mathbf{n}_{[j]} \cdot \mathbf{b})]) \tilde{\mathbf{K}}_{[j]}^+ + (1 - \exp[-\imath(\mathbf{n}_{[j]} \cdot \mathbf{b})]) \tilde{\mathbf{K}}_{[j]}^- \Big],$$

$$B_0(\mathbf{b}) = \eta^2 \kappa_{ae} + \sum_{\mathcal{P}_{[j]}} \Big[(1 + \exp[\imath(\mathbf{n}_{[j]} \cdot \mathbf{b})]) \tilde{K}_a + (1 - \exp[\imath(\mathbf{n}_{[j]} \cdot \mathbf{b})]) \tilde{K}_\ell +$$

$$+ (1 + \exp[-\imath(\mathbf{n}_{[j]} \cdot \mathbf{b})]) \tilde{K}_a + (1 - \exp[-\imath(\mathbf{n}_{[j]} \cdot \mathbf{b})]) \tilde{K}_\ell \Big]. \tag{21}$$

Taking into account the quadrilateral topology of figure 1 for the beam lattice metamaterial, complex-
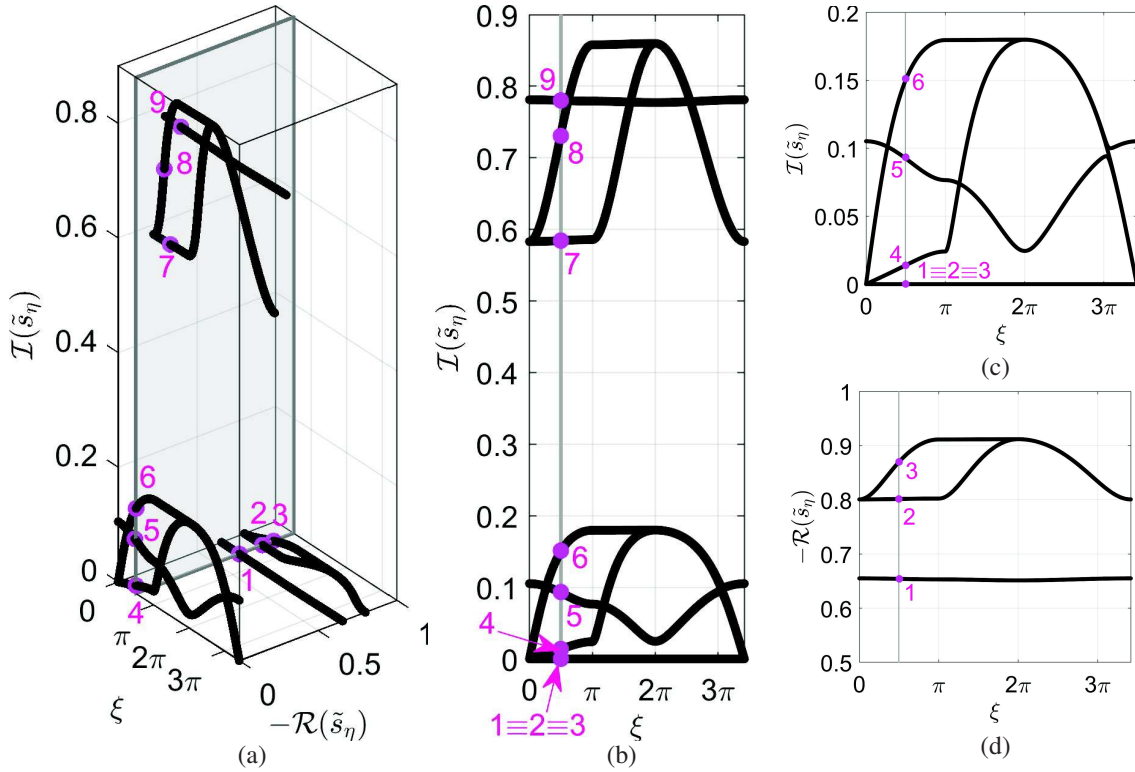

Figure 2: (a) 3D complex frequency spectrum obtained for the beam lattice metamaterial having parameters specified in Section 2.2. Dissecting it with the plane $\xi = \pi/2$, spectral branches are ordered in increasing order according to the value of $\mathcal{I}(\tilde{s}_\eta)$. (b) Two-dimensional view of the complex frequency spectrum in the plane $\{\mathcal{I}(\tilde{s}_\eta); \xi\}$. (c) Zoomed view of the frequency spectrum in the plane $\{\mathcal{I}(\tilde{s}_\eta); \xi\}$ with $0 \le \mathcal{I}(\tilde{s}_\eta) \le 0.2$. (d) Zoomed view of the pure-damping spectral branches in the plane $\{\mathcal{R}(\tilde{s}_\eta); \xi\}$ with $0.5 \le -\mathcal{R}(\tilde{s}_\eta) \le 1$.

valued spectrum obtained solving the eigenvalue problem (19) is represented in figure 2, where the real and imaginary components of the normalized frequency $\tilde{s}_\eta = \tilde{s}/\eta$, denoted as $\mathcal{R}(\tilde{s}_\eta)$ and $\mathcal{I}(\tilde{s}_\eta)$, respectively, are computed in terms of the curvilinear abscissa $\xi \in [0, \pi(2 + \sqrt{2})]$. This last spans the closed boundary of triangular subdomain $\mathcal{B}_1 \subset \mathcal{B}$, where $\mathcal{B} = [-\pi, \pi] \times [-\pi, \pi]$ denotes the dimensionless first Brillouin zone and $\mathcal{B}_1$ has vertices pointed by dimensionless wave vectors $\mathbf{b}_1 = (0 \ 0)^T$, $\mathbf{b}_2 = (\pi \ 0)^T$, and $\mathbf{b}_3 = (\pi \ \pi)^T$. Considering for mechanical material parameters the values $\alpha = 1, \beta_d = \beta_a = 2, \chi_1 = 3/10, \chi_2 = 1/10, \kappa_{ae} = 1/100, \kappa_{de} = 1/5, \mu = 9/100, \varrho^2 = 2, \tilde{t}_r = 4/5$ and $\delta = 1$, a progressive number going from 1 to 9 is associated to each obtained curve dissecting the three-dimensional spectrum by means of the plane $\xi = \pi/2$ in order to clarify what is done next. It is worth mentioning that the number of complex eigenvalues computed from (19) with $N_p = 1$ is $n_e = 15$ (disregarding the non admissible multiple solution $\tilde{s} = -\eta/\tilde{t}_r$ that violates

the non-singularity condition) and that the six missing curves in figure (2) are the complex conjugate ones of curves 4-9, thus having a negative imaginary part of $\tilde{s}_\eta$. Curves $1-3$ lie in the high damping range of the real plane and they can be referred to as pure-attenuation or pure-damping spectral branches. Curves $4-6$ in the low-frequency range correspond to spectral branches of weak attenuation because of the small values of $\mathcal{R}(\tilde{s}_\eta)$ characterizing them. Finally, curves $7-9$ represent the strong attenuation spectral branches reflecting the effect of the attenuation due to viscoelastic coupling. They lie in the high-frequency range and are characterized by non-negligible real values of the complex frequency. In the following, a multi-objective optimization technique based on principal component analysis is presented in order to obtain an approximately optimal design for the metafilter at hand.

3. Computational spectral design

As mentioned above, due to the symmetry of the Floquet-Bloch spectrum with respect to the imaginary axis, only the frequency curves with nonnegative imaginary parts are considered. Such curves are ordered nondecreasingly according to their imaginary parts. In the case of intersections of the imaginary parts, a locally arbitrary order is adopted for the intersected curves (e.g., a lexicographic order, or one based on the real parts of such curves), without changing the results of the successive analysis. Indeed, the band gap and pass band defined in the following paragraphs involve only the imaginary parts of the frequency curves.

For a positive integer k, the amplitude of the (possible) band gap between the k-th and $(k+1)$-th frequencies is determined as the difference $\Delta\tilde{s}_\eta^{BG_{k,k+1}}$ between the minimum of the imaginary part of the $(k+1)$-th frequency (higher limit) and the maximum of the imaginary part of the k-th frequency (lower limit) over the nondimensional wavevector $\mathbf{b} \in \mathcal{B}$. In order for $\Delta\tilde{s}_\eta^{BG_{k,k+1}}$ to be really a bandgap, the condition $\Delta\tilde{s}_\eta^{BG_{k,k+1}} \geq 0$ has to be met. In the following, the band gap $\Delta\tilde{s}_\eta^{BG_{6,7}}$ between the 6-th and 7-th frequencies is considered, having imposed the constraint $\Delta\tilde{s}_\eta^{BG_{6,7}} \geq 0$ (or, equivalently, the constraint $-\Delta\tilde{s}_\eta^{BG_{6,7}} \leq 0$).

Similarly, for two positive integers k_1 and k_2, the amplitude of the (possible) pass band between the k_1-th and (k_1+k_2)-th frequencies is determined as the difference $\Delta\tilde{s}_\eta^{PB_{k_1,k_1+k_2}}$ between the maximum of the imaginary part of the (k_1+k_2)-th frequency (higher limit) and the minimum of the imaginary part of the k_1-th frequency (lower limit) over the nondimensional wavevector $\mathbf{b} \in \mathcal{B}$. In order for $\Delta\tilde{s}_\eta^{PB_{k_1,k_1+k_2}}$ to be really a pass band, no band gap between the k_1-th and (k_1+k_2)-th frequencies can occur. In other words, for all $k \in \{k_1, k_1+1, \dots, k_1+k_2-1\}$, the condition $\Delta\tilde{s}_\eta^{BG_{k,k+1}} \leq 0$ has to be met. In the following, the pass band $\Delta\tilde{s}_\eta^{PB_{7,9}}$ between the 7-th and 9-th frequencies is considered, having imposed the constraints $\Delta\tilde{s}_\eta^{BG_{7,8}} \leq 0$ and $\Delta\tilde{s}_\eta^{BG_{8,9}} \leq 0$. The computational spectral design targeted at achieving the optimal filtering performance of the square lattice metamaterial with viscoelastic resonators (optimal metafilter) can be physically oriented at obtaining the largest multiplicative trade-off between the band gap $\Delta\tilde{s}_\eta^{BG_{6,7}}$ and the pass band $\Delta\tilde{s}_\eta^{PB_{7,9}}$, likewise in [73]. Denoting with $\mathbf{d} \in \mathcal{D} \subseteq \mathbb{R}^d$ the d-dimensional vector collecting all the real-valued microstructural parameters that can be selected as optimizable variables, the optimal filtering performance can be mathematically formalized as solving the following constrained maximization problem

$$\underset{\mathbf{d}\in\mathcal{D}\subset\mathbb{R}^d,\mathbf{g}(\mathbf{d})\leq\mathbf{0}}{\text{maximize}} \ J(\mathbf{d}) \doteq \Delta\tilde{s}_\eta^{BG_{6,7}}(\mathbf{d})\,\Delta\tilde{s}_\eta^{PB_{7,9}}(\mathbf{d})\,, \tag{22}$$

where the 3 components of the vector-valued function $\mathbf{g} : \mathcal{D} \to \mathbb{R}^3$ are defined as

$$g_1(\mathbf{d}) \doteq -\Delta\tilde{s}_\eta^{BG_{6,7}}(\mathbf{d})\,, \tag{23}$$

$$g_2(\mathbf{d}) \doteq \varDelta \tilde{s}_\eta^{BG_{7,8}}(\mathbf{d}),$$ (24)

$$g_3(\mathbf{d}) \doteq \varDelta \tilde{s}_\eta^{BG_{8,9}}(\mathbf{d}).$$ (25)

Problem (22) is a nonlinear optimization problem [74, 75]. Its connections with multi-objective optimization and Pareto optimality are discussed in Section A.3 of the supplementary material. The motivation for the introduction of the constraint $\mathbf{g}(\mathbf{d}) \leq \mathbf{0}$ is that it makes $\varDelta \tilde{s}_\eta^{BG_{6,7}}(\mathbf{d})$ and $\varDelta \tilde{s}_\eta^{PB_{7,9}}(\mathbf{d})$ be really a band gap and a pass band, respectively, as already discussed above.

A second optimization problem, in which only the pass band is maximized, is also considered later in the work:

$$\underset{\mathbf{d} \in \mathcal{D} \subset \mathbb{R}^d, \mathbf{g}(\mathbf{d}) \leq \mathbf{0}}{\text{maximize}} \; J_2(\mathbf{d}) \doteq \varDelta \tilde{s}_\eta^{PB_{7,9}}(\mathbf{d}).$$ (26)

The admissible subset $\mathcal{D}$ is the closure of an open and bounded set, and accounts for all the inequality constraints of the optimization problem that do not involve its Floquet-Bloch spectrum. These include both the admissible range of every single parameter (*box constraints*) and the geometric or mechanical inter-parameter relationships (*internal constraints*). All the other constraints, which involve the Floquet-Bloch spectrum, and whose evaluation is more expensive from a computational point of view, are reported as $\mathbf{g}(\mathbf{d}) \leq \mathbf{0}$ (see equations (23)-(25)). It may be worth remarking that, since the bounded changes in the $\mathbf{d}$-value do not topologically modify the periodic microstructure of the metamaterial, the optimization problems considered here do not fall in the widely explored category of topology optimization problems [76].

3.1. Proposed method: PCA-based penalized optimization

From the methodological viewpoint, the leading idea to address the microstructural optimization problem (22) by means of a PCA-based penalized optimization approach, which is essentially motivated by the high computational cost of evaluating the objective function $J(\mathbf{d})$ and each component of the constraint function $\mathbf{g}(\mathbf{d})$ for each admissible choice of the vector $\mathbf{d}$ (a similar issue arises for the modified optimization problem (26)). In the case of the objective function of the optimization problem (22), this is mainly motivated by the high resolution needed to determine the dispersion functions in the entire $\mathcal{B}$-domain in order to compute the band gap and pass band, as also discussed in the case of other similar optimization problems [77]. In this context, an analogous additional computational effort is needed to evaluate the vector-valued function $\mathbf{g}(\mathbf{d})$ for each choice of the vector $\mathbf{d}$. All this reflects also in a high computational cost needed to evaluate numerically the gradient of the objective function $J(\mathbf{d})$, and the gradient of each component of $\mathbf{g}(\mathbf{d})$. Such a computational cost is proportional to the dimension d.

To address the issues above, the adopted optimization approach is based on replacing, for some large positive penalty parameter φ, the optimization problem (22) with the penalized optimization problem

$$\underset{\mathbf{d} \in \mathcal{D} \subset \mathbb{R}^d}{\text{maximize}} \; J_\varphi(\mathbf{d}) \doteq J(\mathbf{d}) - \varphi p(\mathbf{d}),$$ (27)

where $p : \mathcal{D} \to \mathbb{R}$ is a penalty function which penalizes the violation of the constraint $\mathbf{g}(\mathbf{d}) \leq \mathbf{0}$, and is defined as follows:

$$p(\mathbf{d}) = \max\{g_1(\mathbf{d}), g_2(\mathbf{d}), g_3(\mathbf{d}), 0\}.$$ (28)
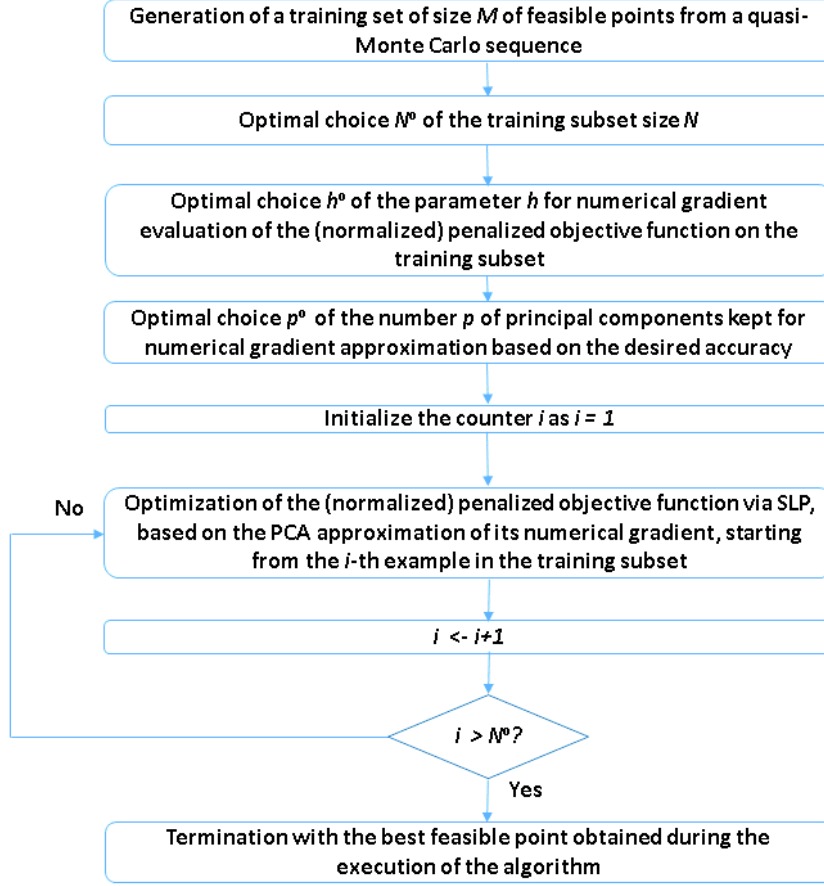
10

Figure 3: Flowchart of the proposed PCA-based penalized optimization algorithm.

Then, to do the optimization numerically, a suitable iterative gradient-based optimization algorithm (namely, Sequential Linear Programming, or SLP) is applied. Instead of using the true gradient of the penalized objective function $J_\varphi(\mathbf{d})$, an approximation of that gradient is used (after replacing the vector $\mathbf{d}$ with its suitable normalization $\mathbf{d}'$, as detailed in the following), based on PCA applied to its suitably sampled field of gradient directions. In the specific case, gradient directions are used instead of gradients, in order to reduce the influence of the penalty parameter φ on the results (as the penalty part $-\varphi p(\mathbf{d})$ of the penalized objective $J_\varphi(\mathbf{d})$ may dominate the other part $J(\mathbf{d})$, for a vector $\mathbf{d} \in \mathcal{D}$ for which the constraint $\mathbf{g}(\mathbf{d}) \leq \mathbf{0}$ is not satisfied).

The proposed algorithm is illustrated in figure 3 and can be synthesized as follows. First, each component of the admissible vector $\mathbf{d}$ is mapped affinely into the interval $[0, 1]$, where 0 corresponds to the minimum value of that component achieved on $\mathcal{D}$, and 1 to its maximum value. The so-obtained normalizations of $\mathbf{d}$ and $\mathcal{D}$ are referred in the following as $\mathbf{d}'$ and $\mathcal{D}'$, respectively. Such normalizations are performed in order to give a-priori the same importance to each component of the admissible (normalized) vector when PCA is applied to the sampled gradient field of the penalized objective function, expressed now as a function $J_\varphi(\mathbf{d}')$. Then, a low-discrepancy Sobol' sequence [78] is used to generate a training

sample set $\mathcal{S}$ of M admissible elements (or *points*) $\mathbf{d}'_i \in \mathcal{D}'$, for $i = 1, \ldots, M$. These are the first M elements of the sequence that also satisfy the constraint $\mathbf{g}(\mathbf{d}') \le \mathbf{0}$ (expressed now in terms of the vector $\mathbf{d}'$ of normalized variables). At this point, several statistics are computed, starting from the M values $\mathbf{d}'_i$. Specifically, centered difference approximations of the components of the gradient $\nabla J_\varphi(\mathbf{d}')$ of the penalized objective function $J_\varphi(\mathbf{d}')$ are computed, for several choices of the stepsize $\epsilon = 10^{-h}$ (where $-h$ represents the stepsize order of magnitude). These approximations are called numerical gradients in the following and are denoted as $\nabla_h J_\varphi(\mathbf{d}'_i)$. Then, for $N = 1, \ldots, M$, PCA is applied to the centered sampled field of numerical gradient directions $\{\nabla_h J_\varphi(\mathbf{d}'_i)/\|\nabla_h J_\varphi(\mathbf{d}'_i)\|_2\}_{i=1}^N$ (i.e., the empirical mean $1/N \sum_{i=1}^N \nabla_h J_\varphi(\mathbf{d}'_i)/\|\nabla_h J_\varphi(\mathbf{d}'_i)\|_2$ of the numerical gradient directions $\nabla_h J_\varphi(\mathbf{d}'_i)/\|\nabla_h J_\varphi(\mathbf{d}'_i)\|_2$ is subtracted from all such numerical gradient directions before applying PCA to them). Finally, the optimal number N° is chosen as the minimal training subset size N for which the eigenvalues obtained by PCA applied to the centered sampled field of numerical gradient directions do not change significantly by increasing that value (independently of the value of the parameter h used for numerical gradient evaluation). As a successive step, the optimal stepsize $\epsilon^\circ = 10^{-h^\circ}$ is chosen, by applying the rule of thumb $\epsilon^\circ = \sqrt[3]{u}$ reported in Section A.4 of the supplementary material, where u is the machine precision. As an additional check of optimality of the related value $h^\circ = \log_{10}(\epsilon^\circ)$, the quantity

$$f^\circ(N, h) = \lim_{\Delta h \to 0} \frac{1}{N^\circ} \sum_{i=1}^{N^\circ} \left\| \frac{\nabla_{h+\Delta h} J_\varphi(\mathbf{d}'_i)}{\|\nabla_{h+\Delta h} J_\varphi(\mathbf{d}'_i)\|_2} - \frac{\nabla_h J_\varphi(\mathbf{d}'_i)}{\|\nabla_h J_\varphi(\mathbf{d}'_i)\|_2} \right\|_2$$

is computed and minimized over h, to confirm that $-h^\circ$ is the optimal stepsize order of magnitude also for this minimization problem (i.e., loosely speaking, that the directions of the numerical gradients are highly stable for this choice of h). This check is motivated by the fact that closed-form expressions for the exact (non-numerical) gradient directions are not available. Next, the normalized penalized objective function $J_\varphi(\mathbf{d}')$ is maximized on $\mathcal{D}'$, using a gradient-based iterative optimization algorithm, namely SLP with an adaptive trust region, likewise in [77] (details of that algorithm are provided therein). The difference with respect to the implementation presented in [77] is that at each iteration of the algorithm, which is associated with a feasible choice of $\mathbf{d}' \in \mathcal{D}'$, instead of evaluating the numerical gradient $\nabla_h J_\varphi(\mathbf{d}')$, one computes its projection on the (at most) $(p^\circ + 1)$-dimensional subspace generated by both the average

$$\mathbf{a}^\circ = \frac{1}{N^\circ} \sum_{i=1}^{N^\circ} \frac{\nabla_h J_\varphi(\mathbf{d}'_i)}{\|\nabla_h J_\varphi(\mathbf{d}'_i)\|_2}$$

of the numerical gradient directions and the selected p° principal directions (the average of the numerical gradient directions is re-introduced here, as it is clearly important for a good reconstruction of the numerical gradient directions through their projections on the selected subspace). The procedure above is repeated by initializing the SLP algorithm N° times, each time using as initialization a different element $\mathbf{d}'_i$ generated from the Sobol' sequence. Finally, the normalized point $\mathbf{d}'_d$ corresponding to the largest original objective value $J(\mathbf{d}')$ computed during all the iterations is mapped back to the corresponding unnormalized point $\mathbf{d}_d$ (applying the inverse of the affine map used to generate the normalized points $\mathbf{d}'$ starting from the unnormalized points $\mathbf{d}$). This point $\mathbf{d}_d$ is taken as the numerical solution to the band gap optimization problem (22). Consequently, $\mathbf{d}_d$ can be referred to as *best design point* in the admissible parameter space. It is worth observing that, by increasing the sample size M, the algorithm convergence to the optimal value of the objective function is guaranteed by the low-discrepancy of the Sobol' sequence with respect to the unit hypercube in $\mathbb{R}^d$. A similar algorithm is used for the second optimization problem (26), for which the

Table 1: Box constraining limits, design values of the metamaterial parameters, and corresponding band gap and pass band amplitudes for $\varphi = 1000$.

	β_a	χ_1	χ_2	κ_{ae}	κ_{de}	μ	ρ	$\tilde{t}_r$	$\Delta\tilde{s}_\eta^{BG_{6,7}}$	$\Delta\tilde{s}_\eta^{PB_{7,9}}$
$\mathbf{d}^{\min}$	$\frac{1}{100}$	$\frac{1}{10}$	$\frac{1}{10}$	$\frac{1}{1000}$	$\frac{1}{1000}$	$\frac{1}{50}$	$\frac{1}{10}$	$\frac{1}{1000}$	–	–
$\mathbf{d}_{\text{base case}}$	2	0.3	0.1	0.01	0.2	0.09	2	0.8	0.4030	0.2768
$\mathbf{d}^{\circ}_{\text{problem (22), no PCA}}$	6.1786	0.3207	0.1425	0.0098	0.1000	0.1000	9.9998	0.8356	0.4789	0.3562
$\mathbf{d}^{\circ}_{\text{problem (22)},p^\circ=3}$	6.3246	0.4200	0.2000	0.0260	0.1000	0.1000	7.0912	0.8166	0.4761	0.3467
$\mathbf{d}^{\circ}_{\text{problem (26), no PCA}}$	8.7810	0.4068	0.1941	0.0024	0.0790	0.0999	9.9039	0.6368	0.0046	0.7597
$\mathbf{d}^{\circ}_{\text{problem (26)},p^\circ=3}$	7.8651	0.4196	0.1871	0.0044	0.0915	0.1000	9.5582	0.6401	0.0528	0.7259
$\mathbf{d}^{\max}$	10	$\frac{1}{2}$	$\frac{1}{2\sqrt{2}}$	$\frac{1}{10}$	$\frac{1}{10}$	$\frac{1}{10}$	10	1	–	–

penalized objective function becomes $J_2(\mathbf{d}) - \varphi p(\mathbf{d})$ and $p(\mathbf{d})$ is defined as above. In Section A.1 of the supplementary material, a detailed theoretical motivation of the proposed method can be found.

4. Results and discussion

In the following, results obtained from the application of the multi-objective optimization technique via PCA presented in Section 3, are illustrated with the aim of obtaining an approximately optimal design for the beam lattice metamaterial described in Section 2. In the specific case, the vector $\mathbf{d}$ of design parameters has the form

$$\mathbf{d} = (\beta_a \ \chi_1 \ \chi_2 \ \kappa_{ae} \ \kappa_{de} \ \mu \ \rho \ \tilde{t}_r)^\top .$$

The other parameters have been fixed to the following values $\beta_d = \beta_a$, $\alpha = \delta = \eta = 1$. The admissible region $\mathcal{D} \subset \mathbb{R}^d$ is formed by applying to each component of the vector $\mathbf{d}$ the following constraints

$$d_j^{min} \leq d_j \leq d_j^{max}, \quad \forall j \in [1, d]. \tag{29}$$

Internal constraints are expressed as

$$\mu \leq \frac{1}{4} \frac{\chi_1}{1 - 2\chi_1}, \tag{30}$$

$$\chi_2 \leq \frac{\chi_1}{2} . \tag{31}$$

Table 1 reports the lower and upper bounds on the components of the vector $\mathbf{d}$, together with their values achieved in correspondence to some choices of $\mathbf{d}$ introduced in the following. The associated band gap and pass band amplitudes are also reported in the table. A non-optimized case characterized by the parameter values reported in the second row of Table 1, is considered as a base case ($\mathbf{d}_{\text{base case}}$), and the resulting Floquet-Bloch spectrum is the one plotted in figure 2. In this case, although one gets both a positive band gap and a positive pass band, their amplitudes are not optimized. It is the goal of the proposed algorithm to improve this base case, by finding an optimized choice for the vector of design parameters. The initial steps of the proposed algorithm are illustrated in figure 4. In its left part, it reports the expression

$$f(N, h) \doteq \lim_{\Delta h \to 0} \frac{1}{N} \sum_{i=1}^{N} \left\| \frac{\nabla_{h+\Delta h} J_\varphi(\mathbf{d}'_i)}{\|\nabla_{h+\Delta h} J_\varphi(\mathbf{d}'_i)\|_2} - \frac{\nabla_h J_\varphi(\mathbf{d}'_i)}{\|\nabla_h J_\varphi(\mathbf{d}'_i)\|_2} \right\|_2 \tag{32}$$

as a function of N, for several values of h, whereas its right part reports $f(N, h)$ as a function of h, for several choices of N (in this figure and in the next ones, the penalty parameter φ is chosen to be equal to 1000). Loosely speaking, a small value of $f(N, h)$ means that on the training subset of dimension N, the directions of the numerical gradients do not vary significantly by changing h. The figure highlights that, for the specific case, one gets $N° \simeq 500$, and $h° \simeq 4$. The Mean Squared Error (MSE) of reconstruction of the numerical gradient field on the training subset is illustrated in figure 5, first, as a function $MSE(N)$ of the training subset size N for various choices of the number of principal components kept p, then as a function $MSE(p)$ of p for various choices of N. Here, PCA is applied to the centered sampled field of numerical gradient directions, after removing from each such vector the mean numerical gradient direction $\mathbf{a}°$. Moreover, the focus is on the reconstruction of the original numerical gradient directions, by projecting them on the subspace generated by the mean numerical gradient direction $\mathbf{a}°$ and the first p principal directions obtained, for $p = 0, 1, \ldots, 7$. The figure highlights that $p = 3$ (which corresponds to a dimension $p + 1 = 4$ of the subspace) allows one to achieve an MSE smaller than 0.1 for N larger than 50, whereas this is not possible for smaller values of p (in other words, for $e\% = 10\%$, the optimal choice of p is $p° = 3$). Figure 6 further illustrates the quality of the approximations of the numerical gradients obtained in the case $p° = 3$ of figure 5, proceeding as follows:

1. first, a specific element of the training set is considered (for illustrative purposes, the selected element is one for which the proposed algorithm converges to the largest obtained value of the objective function J, when the algorithm is initialized with that element);
2. then, four planes are considered (one for each subfigure), by fixing all the values of the (normalized) parameters to the ones of the element in item 1), apart from two (normalized) parameters, which are varied (still respecting the constraints of the optimization problem (22));
3. finally, in correspondence with every point belonging to a regular subgrid of feasible points on each plane, one projects on each of those planes: the numerical gradient computed on that feasible point (the resulting projection is colored in blue); its projection on the subspace generated by the mean numerical gradient direction and the $p° = 3$ principal directions kept (the resulting projection is colored in red).

The figure highlights that the quality of the approximation is quite good, as most of the paired directions
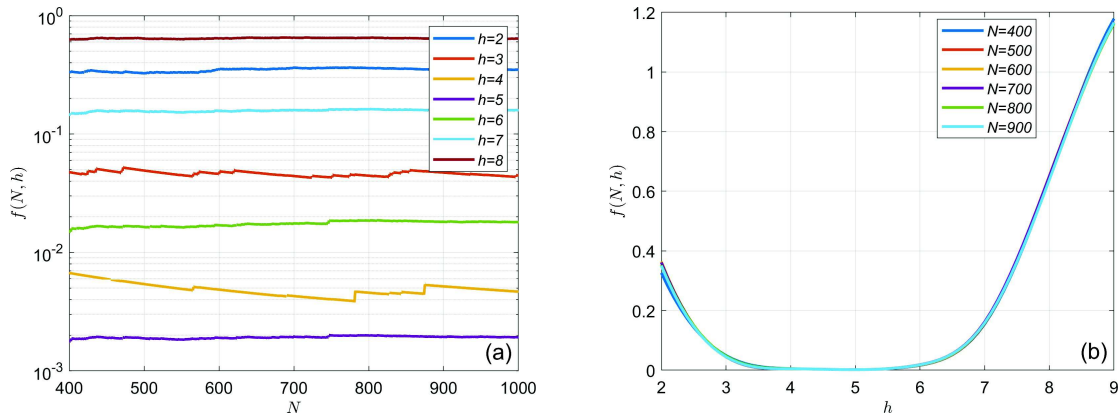

Figure 4: Function $f(N, h)$ defined in eq. (32) as a function of N for different values of h (a) and as a function of h for different values of N (b).
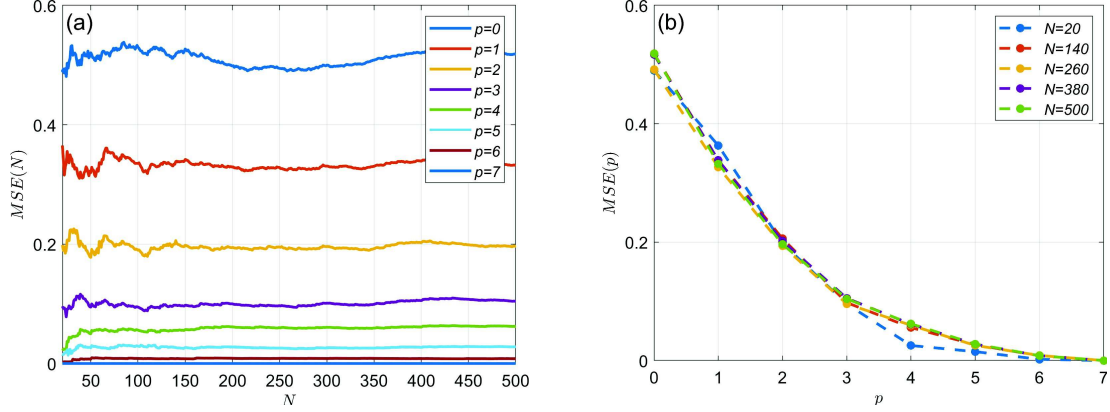
Figure 5: Mean Squared Error (MSE) as a function of N for different values of p (a) and as a function of p for different values of N (b).

form a small acute angle. Figure 7 shows, for several choices of p, the evolution of the penalized objective value $J_\varphi(\mathbf{d}'_{i,iter})$ with respect to $iter$, where i refers to the i-th training subset example from which the proposed algorithm is initialized, and $iter$ the iteration number of SLP (to avoid burdening the notation, the dependence on p is not highlighted in $J_\varphi(\mathbf{d}'_{i,iter})$). Different curve colors correspond to distinct choices of p. Figure 7-(a) shows the whole evolution of $J_\varphi(\mathbf{d}'_{i,iter})$, whereas figure 7-(b) shows its zoom, obtained by restricting the focus on $iter \geq 50$. More precisely, figure 7-(a) focuses on 5 specific initializations that lead to the respective best design point for each among 6 selected values of p, i.e., p° ($p = 3$), two values smaller than p° ($p = 1, 2$), other two values larger than p° ($p = 4, 5$), and its largest possible value ($p = 7$). In two cases, the same initialization is obtained, so it turns out that there are only 5 initializations to consider, instead of 6. Starting from each initialization, the evolution of the penalized objective value $J_\varphi(\mathbf{d}'_{i,iter})$ is reported for each of the 6 selected cases for p. It is worth mentioning that the green horizontal curve in figure 7-(a) refers to a situation in which, for $p = 2$, there is no convergence to the corresponding best design point. However, such a convergence is achieved, still for $p = 2$, for one of the other 4 initializations reported. Since most of the curves in figure 7-(a) are highly overlapped, 7-(b) shows a zoom (near convergence) on the curves that lead to the respective best design point, for each of the 6 cases considered for p. Figure 7-(b) shows that, with the selection $p^\circ = 3$, one achieves almost the same largest penalized objective value as the one obtained by not approximating the numerical gradients through PCA (or equivalently, by choosing $p = 7$, which corresponds to a subspace of the same dimension $p+1 = 8$ as the vector of design parameters). It is also worth observing that, after performing the initial PCA training phase, the computational effort needed for the approximate evaluation of each numerical gradient is reduced by one-half by diminishing from $p+1 = 8$ to $p^\circ+1 = 4$ the dimension of the subspace used to represent such numerical gradients. Figure 7-(c) provides further details on the quality of the approximation of the numerical gradients $\nabla J_\varphi(\mathbf{d}'_{i,iter})$, by plotting $\sin(\vartheta)$ as a function of $iter$, where ϑ is the angle between the numerical gradient $\nabla J_\varphi(\mathbf{d}'_{i,iter})$ and its PCA approximation. The red curve is associated with $\vartheta = 0$, because in that case each $\nabla J_\varphi(\mathbf{d}'_{i,iter})$ coincides with its PCA approximation. Again, the quality of the approximation looks quite good for $p = p^\circ = 3$. Figure 8 reports the Floquet-Bloch spectrum in correspondence of the best design point obtained by solving the optimization problem (22) without applying the PCA approximation (i.e., by choosing $p = 7$). The values of the parameters of such a design point (referred to as $\mathbf{d}^\circ_{problem\,(22),\,no\,PCA}$) are reported in the third
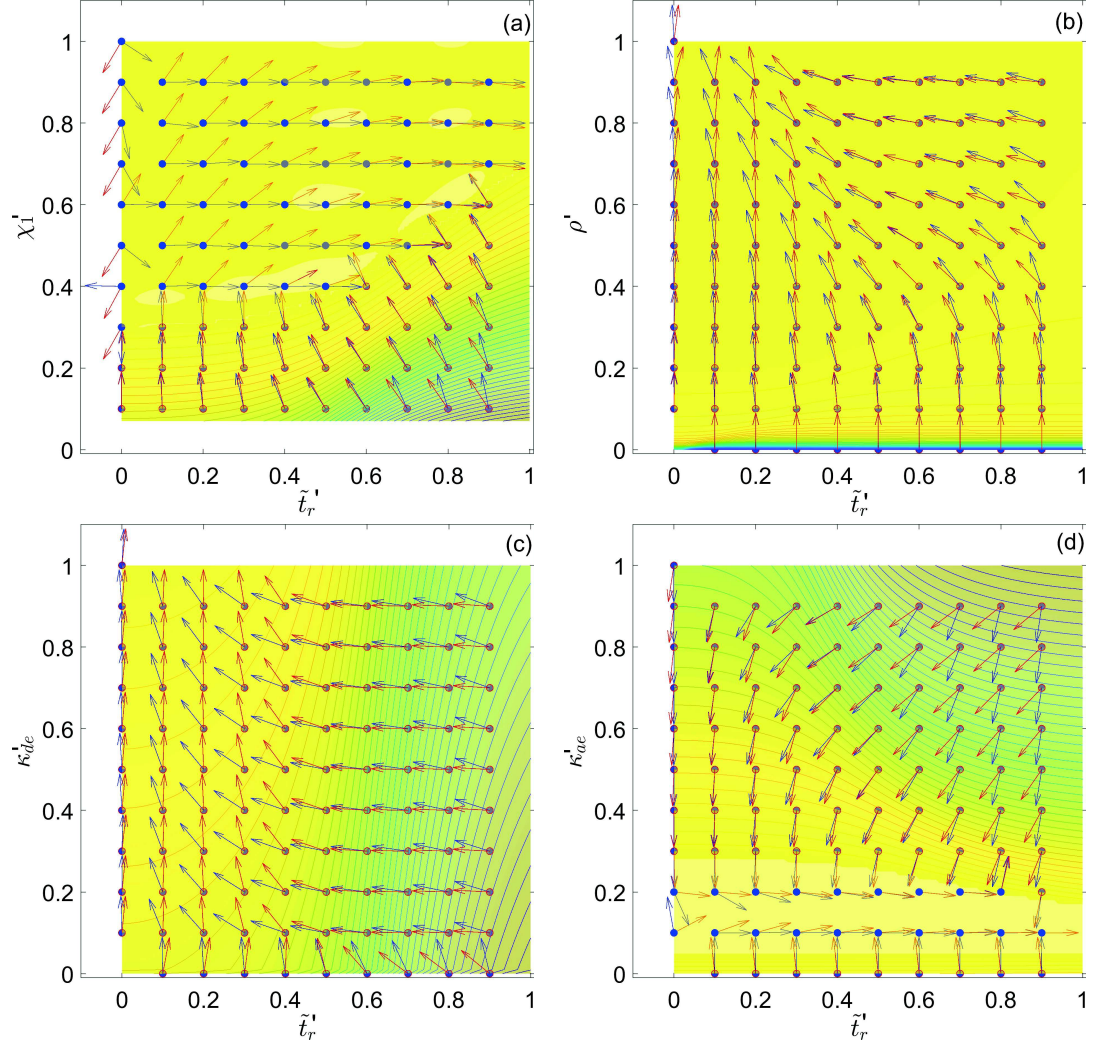
15

Figure 6: Comparison between projections on the planes identified by four couples of normalized parameters of the numerical gradient $\nabla_h \mathbf{J}_\varphi(\mathbf{d}')$ (blue arrows) and projections on the same planes of the approximation of the gradients $\nabla_h \mathbf{J}_\varphi(\mathbf{d}')$ obtained by projecting the numerical gradients onto the subspace generated by the mean direction $\mathbf{a}°$ of the numerical gradient and by $p° = 3$ principal directions (red arrows). The values of the other mechanical parameters refer to the initialization that leads to the optimum in figure 8. (a) $\tilde{t}'_r$ vs χ'_1, (b) $\tilde{t}'_r$ vs ρ', (c) $\tilde{t}'_r$ vs κ'_{de}, (d) $\tilde{t}'_r$ vs κ'_{ae}.

row of Table 1. As one can notice, both the band gap amplitude $\Delta\tilde{s}_\eta^{BG_{6,7}}$ and the pass band one $\Delta\tilde{s}_\eta^{PB_{7,9}}$ have been greatly increased with respect to the base case of figure 2. Similarly, figure 9 reports the Floquet-Bloch spectrum in correspondence of the best design point obtained by solving the optimization problem (22) by applying the PCA approximation (with $p = p° = 3$). The values of the parameters of such a design point (referred to as $\mathbf{d}°_{\text{problem}(22),p°=3}$) are reported in the fourth row of Table 1. A comparison of figures 8 and 9 shows that similar optimized values of the band gap and pass band amplitudes are obtained in these two cases. Figure 10 shows the real and imaginary components of the dimensionless normalized frequency $\tilde{s}_\eta$ obtained in the vertices of $\mathcal{B}_1$, namely $\mathbf{b}_1 = (0\ 0)^T$, $\mathbf{b}_2 = (\pi\ 0)^T$ and $\mathbf{b}_3 = (\pi\ \pi)^T$, by varying only the value of dimensionless relaxation time $\tilde{t}_r$ (from $1/1000$ to 1 as reported in Table 1), whereas all the other parameters values are fixed to the corresponding ones of the best design point. In
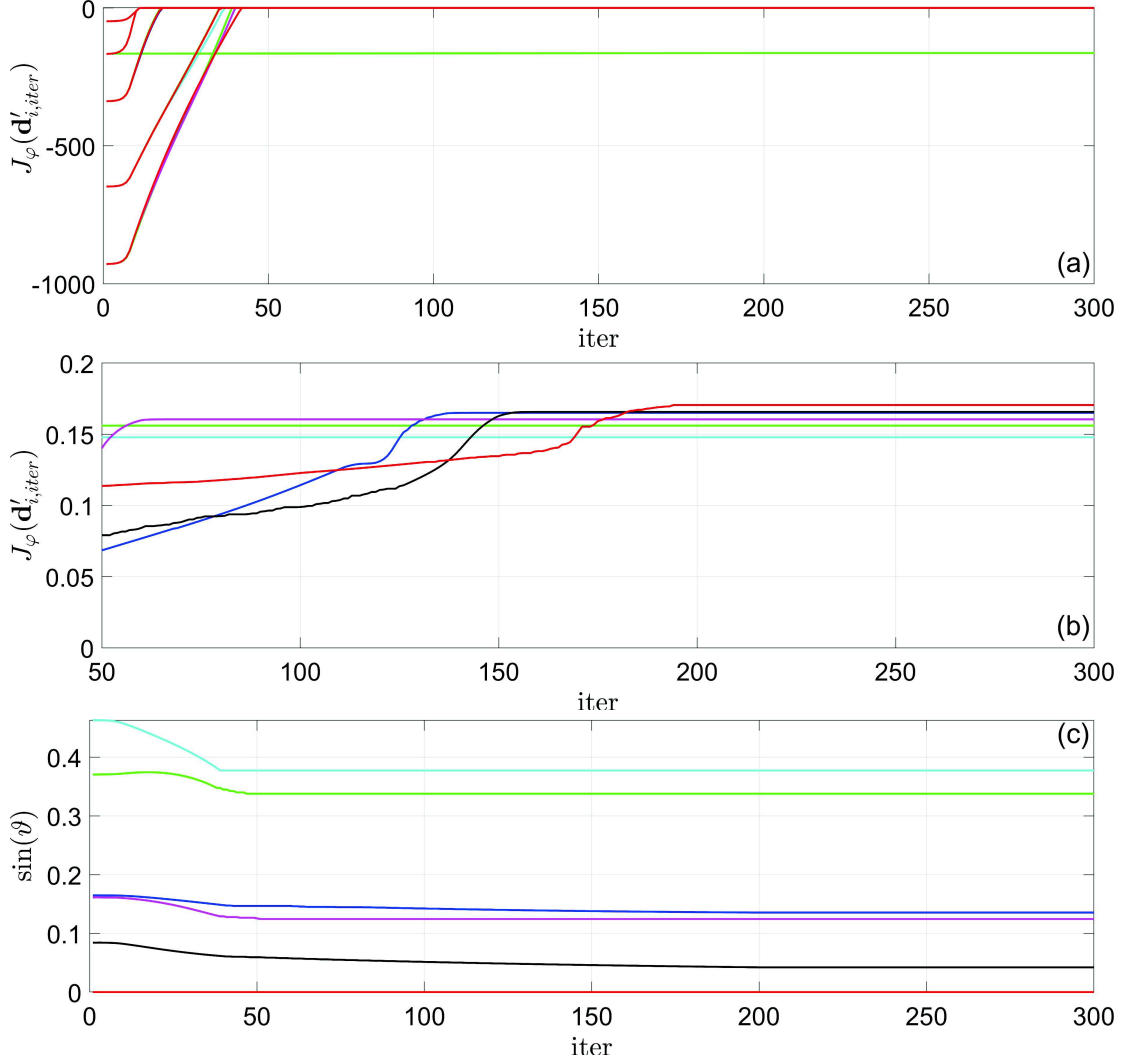
Figure 7: (a) Penalized objective value $J_\varphi(\mathbf{d}'_{i,iter})$ with respect to iteration number $iter$ of SLP. (b) Zoomed view of subfigure (a) for $iter \geq 50$. (c) $sin(\vartheta)$ vs $iter$. Light blue curves refer to $p = 1$, green curves to $p = 2$, magenta curves to $p = 3$, black curves to $p = 4$, blue curves to $p = 5$, and red curves to $p = 7$. Penalty parameter $\varphi = 1000$.

particular, figure 10-(a) refers to design point identified as $\mathbf{d}^\circ_{\mathrm{problem(22),no\,PCA}}$, and figure 10-(b) refers to design point denoted as $\mathbf{d}^\circ_{\mathrm{problem(22)},p^\circ=3}$. Big dots in the figure correspond, for each vertex, to the value of $\tilde{t}_r$ of the corresponding optimized case (the one plotted in figure 8 for points in subfigure 10-(a) and the one plotted in figure 9 for points in subfigure 10-(b)). It is worth mentioning that as $\tilde{t}_r$ increases, curves are swept counterclockwise and that optical branches present points characterized by a vertical tangent, representing the maximum value of $-\mathcal{R}(\tilde{s}_\eta)$ for these curves, or in other words, the maximum damping for the wave propagating inside the medium. Figure 11 reports the Floquet-Bloch spectrum in correspondence to the best design point obtained by solving the optimization problem (26) without applying the PCA approximation (i.e., by choosing $p = 7$). The values of the parameters of such a design point (referred to as $\mathbf{d}^\circ_{\mathrm{problem\,(26),\,no\,PCA}}$) are reported in the fifth row of Table 1. Similarly, figure 12 reports the Floquet-Bloch spectrum in correspondence to the best design point obtained by solving the optimization problem (26)
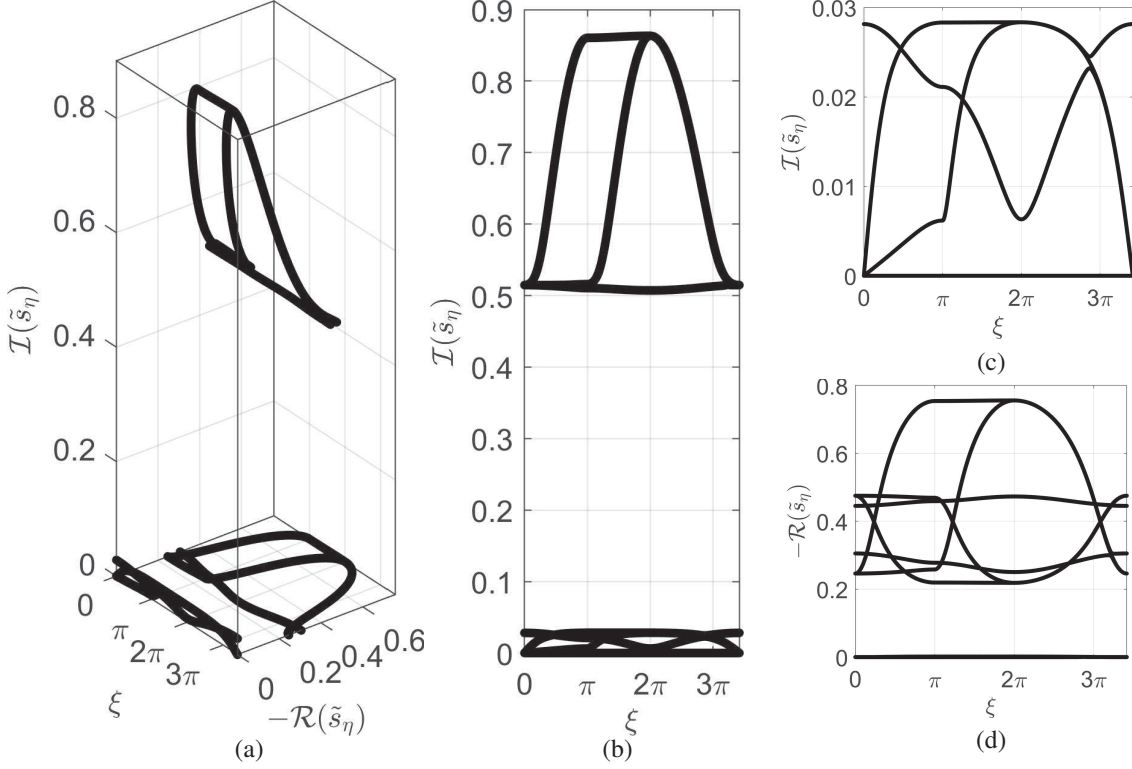
Figure 8: Complex frequency spectrum obtained by solving the optimization problem (22) without the PCA approximation ($p = 7$). The values of the parameters of this design point (denoted as $\mathbf{d}^{\circ}_{\text{problem}(22),\text{no PCA}}$) are the ones reported in the third row of Table 1. (a) 3D Floquet Bloch spectrum, (b) 2D view in the plane $\{\mathcal{I}(\tilde{s}_\eta); \xi\}$, (c) zoomed view in the plane $\{\mathcal{I}(\tilde{s}_\eta); \xi\}$ with $0 \leq \mathcal{I}(\tilde{s}_\eta) \leq 0.03$, (d) 2D view in the plane $\{-\mathcal{R}(\tilde{s}_\eta); \xi\}$.

by applying the PCA approximation (also in this case with $p = p^{\circ} = 3$). The values of the parameters of such a design point (referred to as $\mathbf{d}^{\circ}_{\text{problem}(26),p^{\circ}=3}$) are reported in sixth row of Table 1. Again, a comparison of figures 11 and 12 shows that similar optimized values of the pass band amplitude $\Delta \tilde{s}_\eta^{PB_{7,9}}$ are obtained in these two cases. As clearly noted, in both these cases the amplitude of the pass band $\Delta \tilde{s}_\eta^{PB_{7,9}}$ is greatly increased, specifically almost tripled, with respect to the base case of figure 2, while the band gap amplitude $\Delta \tilde{s}_\eta^{BG_{6,7}}$ is enormously reduced. Optimization problem (26) in fact, is the one in which only $\Delta \tilde{s}_\eta^{PB_{7,9}}$ is maximized and it leads to pass bands much wider, specifically more than doubled, with respect to optimization problem (22), as highlighted from a comparison between figures 11 and 12 and figures 8 and 9. Finally, figure 13-(a) shows the three sections (corresponding to $\mathbf{b}_1 = (0\ 0)^T$, $\mathbf{b}_2 = (\pi\ 0)^T$ and $\mathbf{b}_3 = (\pi\ \pi)^T$) of the Floquet-Bloch spectrum, obtained by varying only the value of the parameter $\tilde{t}_r$ in the range $[1/1000, 1]$, whereas all the other parameter values are fixed to the corresponding ones of the best design point of figure 11. Similarly, figure 13-(b) shows the same three sections of the Floquet-Bloch spectrum, obtained by varying only the value of the parameter $\tilde{t}_r$, whereas all the other parameter values are fixed to the corresponding ones of the best design point of figure 12. Big dots refer, again, to the corresponding optimized case. Optical branches present, also in this case, points with a vertical tangent, corresponding to the maximum damping for the propagating wave. It is worth mentioning that constraint $\mathbf{g}(\mathbf{d}) \leq \mathbf{0}$ is not satisfied for all the points in figure 13, but this is admissible since this figure does not refer
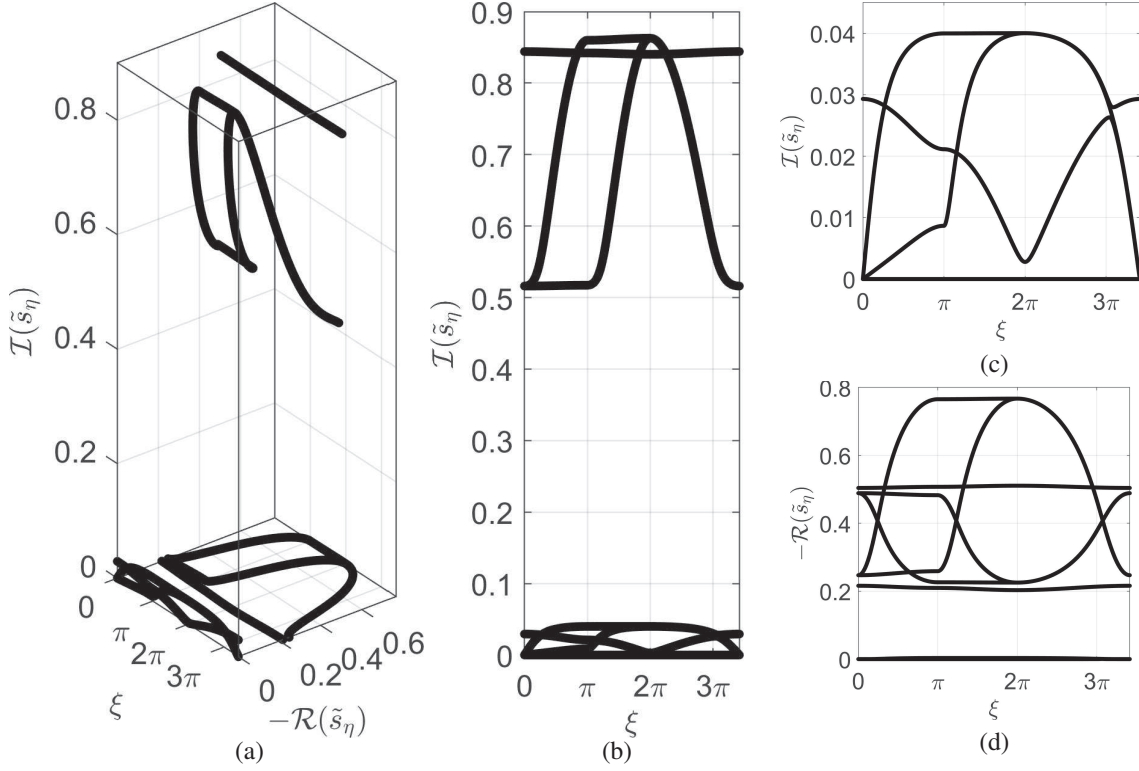
Figure 9: Complex frequency spectrum obtained by solving the optimization problem (22) with the PCA approximation (with $p = p° = 3$). The values of the parameters of this design point (denoted as $\mathbf{d}°_{\text{problem}(22),p°=3}$) are the ones reported in the fourth row of Table 1. (a) 3D Floquet Bloch spectrum, (b) 2D view in the plane $\{\mathcal{I}(\tilde{s}_\eta); \xi\}$, (c) zoomed view in the plane $\{\mathcal{I}(\tilde{s}_\eta); \xi\}$ with $0 \le \mathcal{I}(\tilde{s}_\eta) \le 0.045$, (d) 2D view in the plane $\{-\mathcal{R}(\tilde{s}_\eta); \xi\}$.
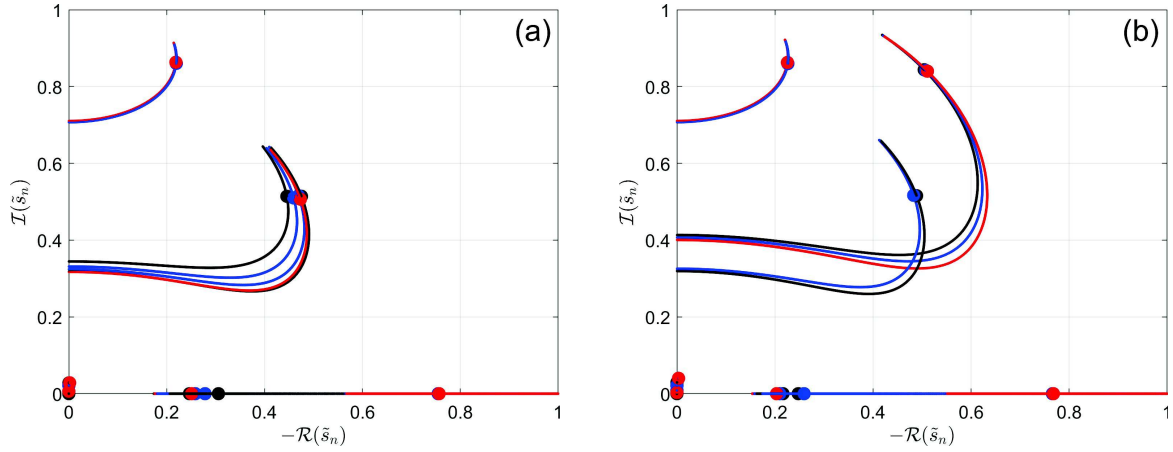

Figure 10: Real and imaginary components of $\tilde{s}_\eta$ for three vertices of the Brillouin zone, namely $\mathbf{b}_1 = (0\ 0)^T$ (black curves), $\mathbf{b}_2 = (\pi\ 0)^T$ (blue curves), and $\mathbf{b}_3 = (\pi\ \pi)^T$ (red curves) obtained by varying parameter $\tilde{t}_r$ in the range $[1/1000, 1]$ while all the other mechanical parameters are kept fixed and equal to the ones of design point denoted as $\mathbf{d}°_{\text{problem}(22),\text{no PCA}}$ (a) and the ones of design point denoted as $\mathbf{d}°_{\text{problem}(22),p°=3}$ (b). Big dots correspond to the respective optimized cases for $\tilde{t}_r$.
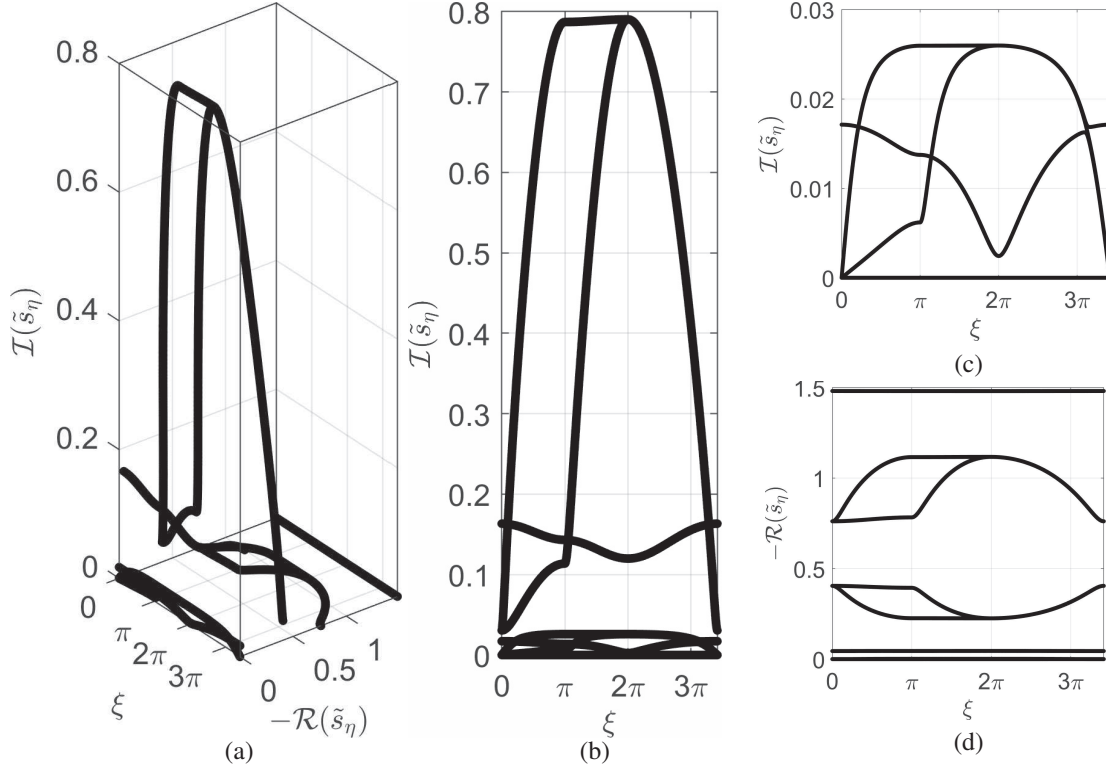
19

Figure 11: Complex frequency spectrum obtained by solving the optimization problem (26) without the PCA approximation ($p = 7$). The values of the parameters of this design point (denoted as $\mathbf{d}^\circ_{\text{problem(26),no PCA}}$) are the ones reported in the fifth row of Table 1. (a) 3D Floquet Bloch spectrum, (b) 2D view in the plane $\{\mathcal{I}(\tilde{s}_\eta); \xi\}$, (c) zoomed view in the plane $\{\mathcal{I}(\tilde{s}_\eta); \xi\}$ with $0 \leq \mathcal{I}(\tilde{s}_\eta) \leq 0.03$, (d) 2D view in the plane $\{-\mathcal{R}(\tilde{s}_\eta); \xi\}$.

to a solution of optimization problem (26).

5. Conclusions

The work is devoted to presenting a machine learning-based technique conceived to obtain an approximately optimal design for a mechanical metamaterial having viscoelastic resonators. Considered planar beam lattice metamaterial is characterized by a periodic microstructure with a centrosymmetric and quadrilateral topology, where local resonance is achieved by means of periodic auxiliary oscillators, coupled with the elastic beam lattice microstructure by means of a viscoelastic phase. Application of a bilateral Laplace transform in time and a bilateral $\mathcal{Z}$-transform in space to the integro-differential equations of motion governing the dynamics of the metamaterial, allows for investigation of the free in-plane propagation of elastic waves in the medium. Dispersion relation has been obtained by solving a rational eigenvalue problem, suitably de-rationalized and transformed into a polynomial one. With the dual purpose of obtaining the largest multiplicative trade-off between the first low-frequency band gap and the optical branches pass band in the metamaterial frequency spectrum on one hand and maximizing only the pass band on the other one, the spectral problem governing the dispersion relation has been tackled as a unilaterally-constrained optimization problem by means of an efficient algorithmic strategy based on Sequential Linear Program-
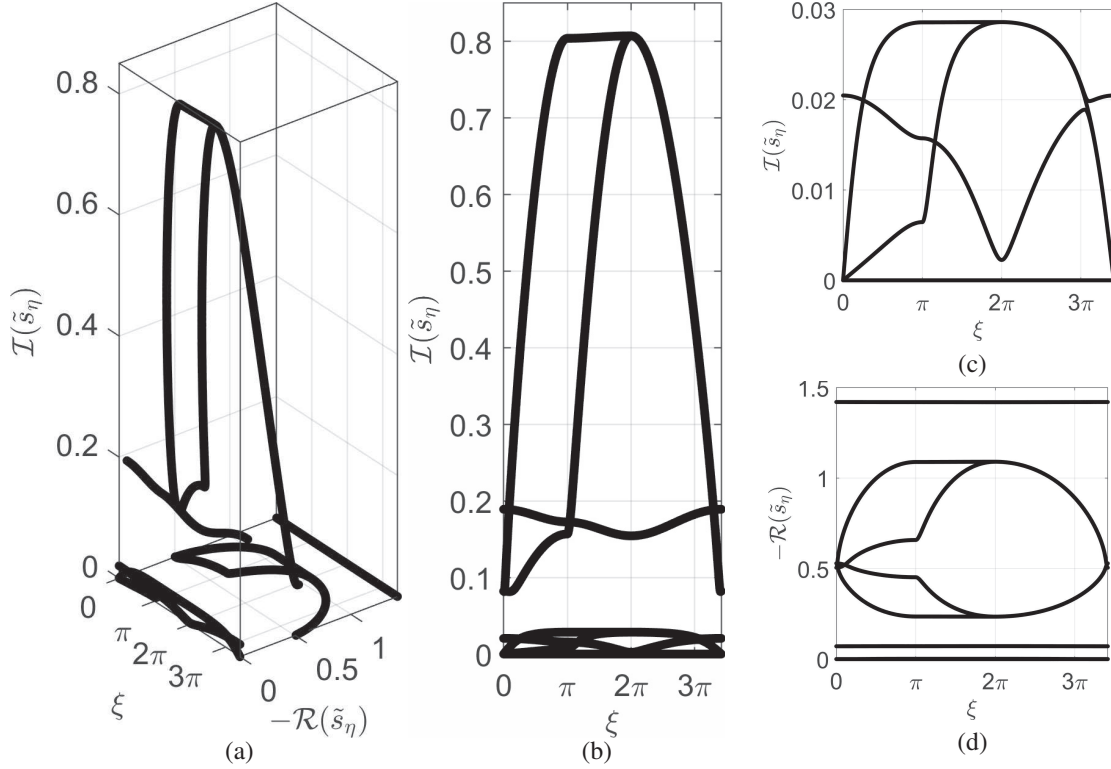
Figure 12: Complex frequency spectrum obtained by solving the optimization problem (26) with the PCA approximation ($p = p° = 3$). The values of the parameters of this design point (denoted as $\mathbf{d}^{\circ}_{\text{problem}(26),p°=3}$) are the ones reported in the sixth row of Table 1. (a) 3D Floquet Bloch spectrum, (b) 2D view in the plane $\{\mathcal{I}(\tilde{s}_\eta); \xi\}$, (c) zoomed view in the plane $\{\mathcal{I}(\tilde{s}_\eta); \xi\}$ with $0 \leq \mathcal{I}(\tilde{s}_\eta) \leq 0.03$, (d) 2D view in the plane $\{-\mathcal{R}(\tilde{s}_\eta); \xi\}$.

ming, which is a gradient-based iterative optimization algorithm. A penalty method has been exploited in order to efficiently replace a subset of constraints (the ones that are more difficult to evaluate from a computational point of view) with the associated term in the penalized objective function. More specifically, an approximation of the optimal design solution has been achieved by means of a PCA-based penalized optimization approach, where PCA is adopted to reduce the number of components of the numerical gradient of the penalized objective function, thus greatly reducing the computational burden required by the multi-dimensionality of the design parameter space. Optimization of dispersion properties has thus been reached in the physically-admissible mechanical parameters range, referred to best design point, and the adopted machine learning method demonstrated to achieve excellent performances in satisfying the desired spectral functionalities. It is important to observe that the best design points obtained using the PCA approximation turned out to have a high quality – expressed in terms of the values achieved by the objective functions of the respective optimization problems (22) and (26) –, comparable to the one achieved without applying that approximation, i.e., by evaluating all the components of the numerical gradients during the execution of Sequential Linear Programming, but at a higher computational cost. This comparison is fair since the number of iterations needed to achieve convergence in these two cases is similar (actually, it is even smaller for the case $p = p° = 3$ with respect to the case $p = 7$, as highlighted from the comparison between the magenta curve and the red curve in figure 7-(b)).

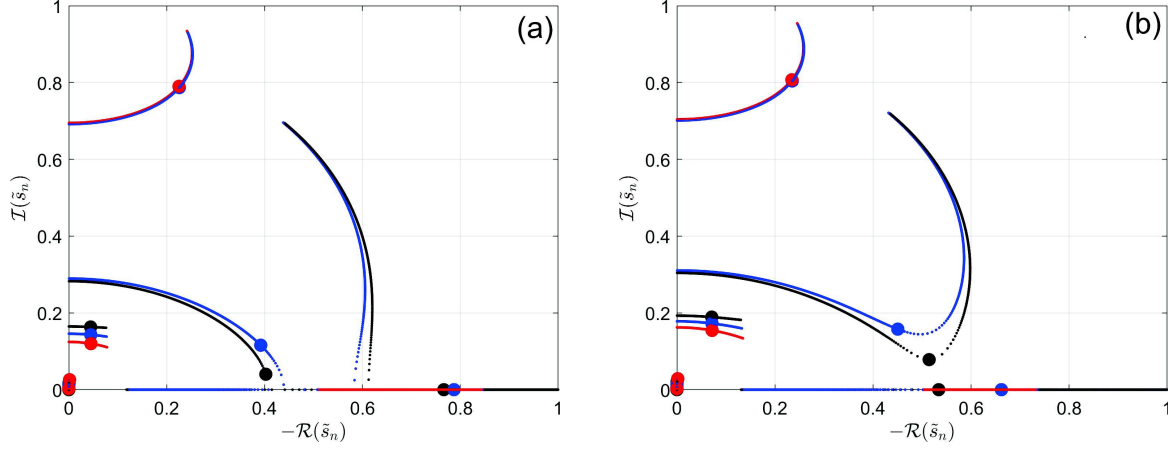Figure 13: Real and imaginary components of $\tilde{s}_\eta$ for three vertices of the Brillouin zone, namely $\mathbf{b}_1 = (0\ 0)^T$ (black curves), $\mathbf{b}_2 = (\pi\ 0)^T$ (blue curves), and $\mathbf{b}_3 = (\pi\ \pi)^T$ (red curves) obtained by varying parameter $\tilde{t}_r$ in the range $[1/1000, 1]$ while all the other mechanical parameters are kept fixed and equal to the ones of design point denoted as $\mathbf{d}^\circ_{\text{problem}(26),\text{no PCA}}$ (a) and the ones of design point denoted as $\mathbf{d}^\circ_{\text{problem}(26),p^\circ=3}$ (b). Big dots correspond to the respective optimized cases for $\tilde{t}_r$.

Acknowledgments

References

[1] L. M. Magid, Mechanical energy flow in crystal lattices, Physical Review 134 (1A) (1964) A158. doi:10.1103/PhysRev.134.A158.

[2] G. Ma, C. Fu, G. Wang, P. Del Hougne, J. Christensen, Y. Lai, P. Sheng, Polarization bandgaps and fluid-like elasticity in fully solid elastic metamaterials, Nature Communications 7 (1) (2016) 1–8. doi:10.1038/ncomms13536.

[3] A. Piccolroaz, A. Movchan, L. Cabras, Dispersion degeneracies and standing modes in flexural waves supported by Rayleigh beam structures, International Journal of Solids and Structures 109 (2017) 152–165. doi:10.1016/J.IJSOLSTR.2017.01.017.

[4] A. Bacigalupo, M. Lepidi, Acoustic wave polarization and energy flow in periodic beam lattice materials, International Journal of Solids and Structures 147 (2018) 183–203. doi:10.1016/j.ijsolstr.2018.05.025.

[5] M. Ruzzene, F. Scarpa, F. Soranna, Wave beaming effects in two-dimensional cellular structures, Smart Materials and Structures 12 (3) (2003) 363–372. doi:10.1088/0964-1726/12/3/307.

[6] P. Martinsson, A. Movchan, Vibrations of lattice structures and phononic band gaps, The Quarterly Journal of Mechanics and Applied Mathematics 56 (1) (2003) 45–64. doi:10.1093/qjmam/56.1.45.

[7] M. L. De Bellis, A. Bacigalupo, Auxetic behavior and acoustic properties of microstructured piezo-electric strain sensors, Smart Materials and Structures 26 (8) (2017) 085037. doi:10.1088/1361-665X/aa7772.

[8] H. W. Park, J. H. Oh, Study of abnormal group velocities in flexural metamaterials, Scientific Reports 9 (1) (2019) 1–13. doi:10.1038/s41598-019-50146-8.

[9] G. Bordiga, L. Cabras, D. Bigoni, A. Piccolroaz, Free and forced wave propagation in a Rayleigh-beam grid: flat bands, dirac cones, and vibration localization vs isotropization, International Journal of Solids and Structures 161 (2019) 64–81. doi:10.1016/j.ijsolstr.2018.11.007.

[10] M. L. De Bellis, A. Bacigalupo, G. Zavarise, Characterization of hybrid piezoelectric nanogenerators through asymptotic homogenization, Computer Methods in Applied Mechanics and Engineering 355 (2019) 1148–1186. doi:10.1016/j.cma.2019.06.040.

[11] A. Zareei, A. Darabi, M. J. Leamy, M.-R. Alam, Continuous profile flexural GRIN lens: Focusing and harvesting flexural waves, Applied Physics Letters 112 (2018) 023901. doi:10.1063/1.5008576.

[12] S.-H. Jo, Y. C. Shin, W. Choi, H. Yoon, B. D. Youn, M. Kim, Double defects-induced elastic wave coupling and energy localization in a phononic crystal, Nano Convergence 8 (1) (2021) 1–13. doi:10.1186/s40580-021-00277-4.

[13] F. Lemoult, N. Kaina, M. Fink, G. Lerosey, Wave propagation control at the deep subwavelength scale in metamaterials, Nature Physics 9 (1) (2013) 55–60. doi:10.1038/nphys2480.

[14] G. Allegri, F. Scarpa, R. Chowdhury, S. Adhikari, Wave propagation in periodically supported nanoribbons: A nonlocal elasticity approach, Journal of Vibration and Acoustics 135 (4) (2013). doi:10.1115/1.4023953.

[15] A. Bacigalupo, L. Gambarotta, Dispersive wave propagation in two-dimensional rigid periodic blocky materials with elastic interfaces, Journal of the Mechanics and Physics of Solids 102 (2017) 165–186. doi:10.1016/j.jmps.2017.02.006.

[16] A. Bacigalupo, L. Gambarotta, Wave propagation in non-centrosymmetric beam-lattices with lumped masses: discrete and micropolar modeling, International Journal of Solids and Structures 118 (2017) 128–145. doi:10.1016/j.ijsolstr.2017.04.010.

[17] L. D'Alessandro, V. Zega, R. Ardito, A. Corigliano, 3D auxetic single material periodic structure with ultra-wide tunable bandgap, Scientific Reports 8 (1) (2018) 2262. doi:10.1038/s41598-018-19963-1.

[18] F. Dal Corso, D. Tallarico, N. V. Movchan, A. B. Movchan, D. Bigoni, Nested Bloch waves in elastic structures with configurational forces, Philosophical Transactions of the Royal Society A 377 (2156) (2019) 20190101. doi:10.1098/rsta.2019.0101.

[19] I. V. Kamotski, V. P. Smyshlyaev, Bandgaps in two-dimensional high-contrast periodic elastic beam lattice materials, Journal of the Mechanics and Physics of Solids 123 (2019) 292–304. doi:10.1016/j.jmps.2018.08.024.

[20] S. Mukherjee, F. Scarpa, S. Gopalakrishnan, Phononic band gap design in honeycomb lattice with combinations of auxetic and conventional core, Smart Materials and Structures 25 (5) (2016) 054011. doi:10.1088/0964-1726/25/5/054011.

[21] Y. Wang, X. Liu, R. Zhu, G. Hu, Wave propagation in tunable lightweight tensegrity metastructure, Scientific Reports 8 (1) (2018) 1–12. doi:10.1038/s41598-018-29816-6.

[22] M. Bruggi, A. Corigliano, Optimal 2D auxetic micro-structures with band gap, Meccanica 54 (13) (2019) 2001–2027. doi:10.1007/s11012-019-00981-w.

[23] Z. P. Wang, L. H. Poh, Y. Zhu, J. Dirrenberger, S. Forest, Systematic design of tetra-petals auxetic structures with stiffness constraint, Materials & Design 170 (2019) 107669. doi:10.1016/j.matdes.2019.107669.

[24] L. Shen, K. Wei, K. Yuan, C. Shi, Z. Li, Z. Wang, A novel metamaterial incorporating both auxeticity and thermal shrinkage, International Journal of Mechanical Sciences 233 (2022) 107650.

[25] Y. Zhu, S. Jiang, Q. Zhang, J. Li, C. Yu, C. Zhang, A novel monoclinic auxetic metamaterial with tunable mechanical properties, International Journal of Mechanical Sciences (2022) 107750.

[26] S. Foteinopoulou, E. N. Economou, C. Soukoulis, Refraction in media with a negative refractive index, Physical Review Letters 90 (10) (2003) 107402. doi:10.1103/PhysRevLett.90.107402.

[27] D. R. Smith, J. B. Pendry, M. C. Wiltshire, Metamaterials and negative refractive index, Science 305 (5685) (2004) 788–792. doi:10.1126/science.109679.

[28] S. A. Ramakrishna, Physics of negative refractive index materials, Reports on Progress in Physics 68 (2) (2005) 449. doi:10.1088/0034-4885/68/2/R06.

[29] W. J. Padilla, D. N. Basov, D. R. Smith, Negative refractive index metamaterials, Materials Today 9 (7–8) (2006) 28–35. doi:10.1016/S1369-7021(06)71573-5.

[30] Y. Pennec, J. O. Vasseur, B. Djafari-Rouhani, L. Dobrzyński, P. A. Deymier, Two-dimensional phononic crystals: Examples and applications, Surface Science Reports 65 (8) (2010) 229–291. doi:10.1016/j.surfrep.2010.08.002.

[31] R. Zhu, X. Liu, G. Hu, C. Sun, G. Huang, A chiral elastic metamaterial beam for broad-band vibration suppression, Journal of Sound and Vibration 333 (10) (2014) 2759–2773. doi:10.1016/j.jsv.2014.01.009.

[32] M. Ouisse, M. Collet, F. Scarpa, A piezo-shunted kirigami auxetic lattice for adaptive elastic wave filtering, Smart Materials and Structures 25 (11) (2016) 115016. doi:10.1088/0964-1726/25/11/115016.

[33] A. Bacigalupo, L. Gambarotta, Chiral two-dimensional periodic blocky materials with elastic interfaces: Auxetic and acoustic properties, Extreme Mechanics Letters 39 (2020) 100769. doi:10.1016/j.eml.2020.100769.

[34] A. Bacigalupo, M. L. De Bellis, M. Vasta, Design of tunable hierarchical waveguides based on fibonacci-like microstructure, International Journal of Mechanical Sciences 224 (2022) 107280. doi:10.1016/j.ijmecsci.2022.107280.

[35] Y. Zeng, L. Cao, S. Wan, T. Guo, Y.-F. Wang, Q.-J. Du, B. Assouar, Y.-S. Wang, Seismic metamaterials: Generating low-frequency bandgaps induced by inertial amplification, International Journal of Mechanical Sciences 221 (2022) 107224.

[36] M. Ma, L. Wang, Reliability-based topology optimization framework of two-dimensional phononic crystal band-gap structures based on interval series expansion and mapping conversion method, International Journal of Mechanical Sciences 196 (2021) 106265.

[37] M. Tyburec, M. Doškář, J. Zeman, M. Kružík, Modular-topology optimization of structures and mechanisms with free material design and clustering, Computer Methods in Applied Mechanics and Engineering 395 (2022) 114977. doi:10.1016/j.cma.2022.114977.

[38] J. E. Cadman, S. Zhou, Y. Chen, Q. Li, On design of multi-functional microstructural materials, Journal of Materials Science 48 (1) (2013) 51–66. doi:10.1007/s10853-012-6643-4.

[39] R. Ramprasad, R. Batra, G. Pilania, A. Mannodi-Kanakkithodi, C. Kim, Machine learning in materials informatics: recent applications and prospects, npj Computational Materials 3 (1) (2017) 1–13. doi:10.1038/s41524-017-0056-5.

[40] W. Ma, F. Cheng, Y. Liu, Deep-learning-enabled on-demand design of chiral metamaterials, ACS Nano 12 (6) (2018) 6326–6334. doi:10.1021/acsnano.8b03569.

[41] W. Wu, W. Hu, G. Qian, H. Liao, X. Xu, F. Berto, Mechanical design and multifunctional applications of chiral mechanical metamaterials: A review, Materials & Design (2019)

107950doi:10.1016/j.matdes.2019.107950.

[42] D. M. Kochmann, J. B. Hopkins, L. Valdevit, Multiscale modeling and optimization of the mechanics of hierarchical metamaterials, MRS Bulletin 44 (10) (2019) 773–781. doi:10.1557/mrs.2019.228.

[43] J. Zhao, Y. Dong, C. Ye, Optimization of residual stresses generated by ultrasonic nanocrystalline surface modification through analytical modeling and data-driven prediction, International Journal of Mechanical Sciences 197 (2021) 106307.

[44] P. C. Kainen, V. Kůrková, M. Sanguineti, Dependence of computational models on input dimension: Tractability of approximation and optimization tasks, IEEE Transactions on Information Theory 58 (2) (2012) 1203–1214. doi:10.1109/TIT.2011.2169531.

[45] R. Bro, A. K. Smilde, Principal component analysis, Analytical Methods 6 (9) (2014) 2812–2831. doi:10.1039/C3AY41907J.

[46] H. Abdi, L. J. Williams, Principal component analysis, Wiley Interdisciplinary Reviews: Computational Statistics 2 (4) (2010) 433–459. doi:10.1002/wics.101.

[47] D. D'Agostino, A. Serani, E. F. Campana, M. Diez, Nonlinear methods for design-space dimensionality reduction in shape optimization, International Workshop on Machine Learning, Optimization, and Big Data. Lecture Notes in Computer Science 10710 (2017) 121–132. doi:10.1007/978-3-319-72926-8_11.

[48] G. Gnecco, A. Bacigalupo, Convex combination of data matrices: PCA perturbation bounds for multi-objective optimal design of mechanical metafilters, Mathematical Foundations of Computing 4 (4) (2021) 253. doi:10.3934/mfc.2021014.

[49] G. Gnecco, A. Bacigalupo, F. Fantoni, D. Selvi, Principal component analysis applied to gradient fields in band gap optimization problems for metamaterials, in: Proceedings of the Sixth International Conference on Metamaterials and Nanophotonics (METANANO 2020), Journal of Physics: Conference Series, Vol. 2015, 2021, article ID 012047, 4 pages. doi:10.1088/1742-6596/2015/1/012047.

[50] G. Tzimiropoulos, S. Zafeiriou, M. Pantic, Subspace learning from image gradient orientations, IEEE Transactions on Pattern Analysis and Machine Intelligence 34 (2012) 2454–2466. doi:10.1109/TPAMI.2012.40.

[51] Z. Liu, X. Zhang, Y. Mao, Y. Zhu, Z. Yang, C. T. Chan, P. Sheng, Locally resonant sonic materials, Science 289 (5485) (2000) 1734–1736. doi:10.1126/science.289.5485.173.

[52] N. Fang, D. Xi, J. Xu, M. Ambati, W. Srituravanich, C. Sun, X. Zhang, Ultrasonic metamaterials with negative modulus, Nature Materials 5 (6) (2006) 452–456. doi:10.1038/nmat1644.

[53] W. Akl, A. Baz, Active acoustic metamaterial with simultaneously programmable density and bulk modulus, Journal of Vibration and Acoustics 135 (3) (2013). doi:doi.org/10.1115/1.4023141.

[54] G. Ma, P. Sheng, Acoustic metamaterials: From local resonances to broad horizons, Science Advances 2 (2) (2016) e1501595. doi:10.1126/sciadv.1501595.

[55] A. Krushynska, V. Kouznetsova, M. Geers, Towards optimal design of locally resonant acoustic metamaterials, Journal of the Mechanics and Physics of Solids 71 (2014) 179–196. doi:10.1016/j.jmps.2014.07.004.

[56] A. Bacigalupo, L. Gambarotta, Simplified modelling of chiral lattice materials with local resonators, International Journal of Solids and Structures 83 (2016) 126–141. doi:10.1016/j.ijsolstr.2016.01.005.

[57] A. Bacigalupo, M. L. De Bellis, D. Misseroni, Design of tunable acoustic metamaterials with periodic piezoelectric microstructure, Extreme Mechanics Letters 40 (2020) 100977. doi:10.1088/1367-

2630/13/11/113010.

[58] J. Jung, S. Goo, J. Kook, Design of a local resonator using topology optimization to tailor bandgaps in plate structures, Materials & Design 191 (2020) 108627. doi:10.1016/j.matdes.2020.108627.

[59] V. Gorshkov, P. Sareh, N. Navadeh, V. Tereshchuk, A. S. Fallah, Multi-resonator metamaterials as multi-band metastructures, Materials & Design 202 (2021) 109522. doi:10.1016/j.matdes.2021.109522.

[60] F. Fantoni, E. Bosco, A. Bacigalupo, Multifield nested metafilters for wave propagation control, Extreme Mechanics Letters 56 (2022) 101885. doi:10.1016/j.eml.2022.101885.

[61] D. Bigoni, S. Guenneau, A. Movchan, M. Brun, Elastic metamaterials with inertial locally resonant structures: Application to lensing and localization, Physical Review B 87 (17) (2013) 174303. doi:10.1103/PhysRevB.87.174303.

[62] A. Bacigalupo, G. Gnecco, M. Lepidi, L. Gambarotta, Optimal design of low-frequency band gaps in anti-tetrachiral lattice meta-materials, Composites Part B 115 (2017) 341–359. doi:10.1016/j.compositesb.2016.09.062.

[63] M. Morvaridi, G. Carta, M. Brun, Platonic crystal with low-frequency locally-resonant spiral structures: wave trapping, transmission amplification, shielding and edge waves, Journal of the Mechanics and Physics of Solids 121 (2018) 496–516. doi:10.1016/j.jmps.2018.08.017.

[64] L. Morini, Y. Eyzat, M. Gei, Negative refraction in quasicrystalline multilayered metamaterials, Journal of the Mechanics and Physics of Solids 124 (2019) 282–298. doi:10.1016/j.jmps.2018.10.016.

[65] F. Vadalà, A. Bacigalupo, M. Lepidi, L. Gambarotta, Free and forced wave propagation in beam lattice metamaterials with viscoelastic resonators, International Journal of Mechanical Sciences 193 (2021) 106129. doi:10.1016/j.ijmecsci.2020.106129.

[66] R. Lakes, Viscoelastic materials, Cambridge university press, 2009. doi:10.1017/CBO9780511626722.

[67] J. R. Ragazzini, L. A. Zadeh, The analysis of sampled-data systems, Transactions of the American Institute of Electrical Engineers, Part II: Applications and Industry 71 (5) (1952) 225–234. doi:10.1109/TAI.1952.6371274.

[68] E. I. Jury, Theory and Application of the z-Transform Method, Wiley, 1964. doi:10.2307/2315992.

[69] Y. Su, Z. Bai, Solving rational eigenvalue problems via linearization, SIAM Journal on Matrix Analysis and Applications 32 (1) (2011) 201–216. doi:10.1137/090777542.

[70] B. P. Brooks, The coefficients of the characteristic polynomial in terms of the eigenvalues and the elements of an n×n matrix, Applied Mathematics Letters 19 (6) (2006) 511–515. doi:10.1016/j.aml.2005.07.007.

[71] F. Fantoni, A. Bacigalupo, Wave propagation modeling in periodic elasto-thermo-diffusive materials via multifield asymptotic homogenization, International Journal of Solids and Structures 196 (2020) 99–128. doi:10.1016/j.ijsolstr.2020.03.024.

[72] F. Fantoni, L. Morini, A. Bacigalupo, M. Paggi, The generalized Floquet-Bloch spectrum for periodic thermodiffusive layered materials, International Journal of Mechanical Sciences 194 (2021) 106178. doi:10.1016/j.ijmecsci.2020.106178.

[73] A. Bacigalupo, G. Gnecco, M. Lepidi, L. Gambarotta, Design of acoustic metamaterials through nonlinear programming, in: International Workshop on Machine Learning, Optimization, and Big Data, Springer, 2016, pp. 170–181. doi:10.1007/978-3-319-51469-7_14.

[74] J. Nocedal, S. J. Wright, Numerical Optimization, Springer, 2006. doi:10.1007/978-0-387-40065-5.

[75] I. M. Bomze, V. F. Demyanov, R. Fletcher, T. Terlaky, Nonlinear Optimization, Springer, 2007. doi:10.1007/978-3-642-11339-0.

[76] W. Li, F. Meng, Y. Chen, Y. F. Li, X. Huang, Topology optimization of photonic and phononic crystals and metamaterials: A review, Advanced Theory and Simulations 2 (7) (2019) 1900017. doi:10.1002/adts.201900017.

[77] A. Bacigalupo, G. Gnecco, M. Lepidi, L. Gambarotta, Machine-learning techniques for the optimal design of acoustic metamaterials, Journal of Optimization Theory and Applications 187 (2020) 630–653. doi:10.1007/s10957-019-01614-8.

[78] R. Zoppoli, M. Sanguineti, G. Gnecco, T. Parisini, Neural Approximation for Optimal Control and Decision, Springer, 2020. doi:10.1007/978-3-030-29693-3.